Coaxial Ferrimagnetic Based Gyromagnetic Nonlinear Transmission Lines as Compact High Power Microwave Sources

by

David V. Reale, B.S.E.E., M.S.E.E.

A Dissertation

In

ELECTRICAL ENGINEERING

Submitted to the Graduate Faculty
of Texas Tech University in
Partial Fulfillment of
the Requirements for
the Degree of

DOCTOR OF PHILOSOPHY

Approved

Dr. John J. Mankowski
Committee Chairman

Dr. James C. Dickens

Dr. Mohammed Saed

Dr. Anton Geiler

Dr. J.-W. Braxton Bragg

Dominick J. Casadonte, Jr.
Interim Dean of the Graduate School

December, 2013

ACKNOWLEDGEMENTS

I would like to thank Dr. John Mankowski for giving me the opportunity to continue my education and for his guidance along the way. I would also like to thank my committee members Dr. James Dickens and Dr. Mohammed Saed, as well as the rest of the ECE and P3E faculty, for their help and ideas. Thank you to Dr. Anton Geiler for helping me on the topics of micromagnetism and magnetic materials and Dr. J.-W. Braxton Bragg for guiding my transition into the field of Nonlinear Transmission Lines. Also, thank you to Dr. Andreas Neuber from whose classes I have learned so very much. To the P^{3}E staff including Joel, Danny, Dino, Lee and Kathryn for all their help over the years.

I would like to extend a special thanks to my friends and colleagues for their ideas, inspirations, and entertaining discussions throughout the years. My success would not be possible without my friends, including Ryan Karhi, William Sullivan III, Jonathan Parson, Patrick Kelly, Nathan Gonsalves, and Rick Solarski.

I would like to thank my friends back home in Massachusetts, Christopher Garvey, David Whalley, and The Whalley family, who made it possible to move to Texas in the first place and always made me feel like I never left home. Lastly, I would like to thank my family, especially my mother Dianna, for their continued support throughout the duration of my studies.

TABLE OF CONTENTS

ABSTRACT

Coaxial ferrimagnetic Nonlinear Transmission Lines (NLTL) can be used as pulsed, solid-state, High Power Microwave (HPM) sources. An NLTL can operate in either pulse sharpening or microwave generation mode depending on the initial magnetization of the ferrimagnetic material and the applied magnetic field. Present research at Texas Tech University is focused on creating an array of NLTLs operating in microwave generation mode for use as a compact HPM system. The microwaves produced by NLTLs are due to the motion of magnetic moments in the ferrimagnetic material through damped gyromagnetic precession. This motion is described by the Landau-Lifshitz Gilbert (LLG) equation and is the primary method for analyzing design requirements. Since the precession frequency is proportional to the applied field, the gyromagnetic ratio constant, and inversely proportional to the phenomenological damping factor, the NLTL is a tunable frequency HPM source. The permeability of the ferrimagnetic material can be altered by applying a biasing magnetic field thereby allowing for an adjustable delay on each line by controlling the phase velocity. The NLTL system uses a pressurized spark gap to generate a 15 kV to 40 kV voltage pulse with a rise time on the order of 2 ns to drive coaxial transmission lines insulated with pressurized sulfur hexafluoride (SF_6). The ferrimagnetic material is in the form of toroidal ferrites around the inner conductor of the coaxial line. The resulting source is frequency adjustable from 1 GHz to 4 GHz with an output power of 40 MW. A two-way transient high power guided combiner was designed and tested and results are presented. An NLTL model was developed using a Finite Element Method (FEM) simulation in COMSOL. The simulation solves the LLG equations for a coaxial geometry allowing for calculation of effective fields and estimation of the operating frequency.

LIST OF FIGURES

LIST OF TABLES

CHAPTER 1

INTRODUCTION TO NONLINEAR TRANSMISSION LINES

High Power Microwave (HPM) sources have an extensive and varied scope of applications including remote sensing (RADAR), electronic warfare, non-lethal weapons, and directed energy systems. Currently e-beam tubes such as magnetrons, klystrons, Traveling Wave Tubes (TWT) and Backward Wave Oscillators (BWO) dominate the high power microwave landscape. While beam tubes are a mature technology they are most commonly fixed frequency sources with a minimum size often dictated by the requirement of vacuum components. Also, significant design work and optimization is required for each source e-beam source. [7, 8].

Ferrimagnetic Nonlinear Transmission Lines (NLTL) offer an alternative to e-beam based HPM sources. They are compact, modular, and easy to construct solid state HPM sources with an adjustable frequency. Multiple NLTLs can be combined into an array to reach power levels in the range of several hundred MW.

1.1 Past Research in the Field of Nonlinear Transmission Lines

A Nonlinear Transmission Line can mean any type of transmission line structure containing a material which exhibits a nonlinear response to an incident field. One of the first and best known cases is the optical Kerr effect in which incident light causes an anisotropic change to the index of refraction of the material, this is an example of a nonlinear dielectric material.

Research interest into NLTLs as we recognize them today began in the 1950s and 1960s and coincided with the recent advent and availability of ferrimagnetic materials. Most of this research was focused on the application of NLTLs as pulse sharpening devices. In pulse sharpening mode the incoherent precession of the magnetic moments saturates the material without creating a propagating microwave signal. The saturated ferrite now has a lower permeability and consequently higher phase velocity for the remainder of the pulse allowing the back end of the pulse to 'catch up' to the leading edge resulting in pulse sharpening. This phenomenon was first explained as an electrical shock front and involved the balancing of dispersion at the edge with the increased energy provided by the now faster back end of the pulse resulting in a traveling standing wave or soliton. This explanation is still applicable to Nonlinear Lumped Element Transmission Lines (NLETL) and explains their behavior very well.

Most of the early work on NLTLs was carried out by Katayev in the 1960s and 1970s focused on pulse sharpening and soliton generation and by Dolan and Seddon from the United Kingdom in the 1990s and early 2000s. A major change occurs in Dolan's work in which the emphasis shifted to the gyromagnetic behavior of NLTL, as opposed to a solitary wave solution. The pulse sharpening behavior was explained using a gyromagnetic approach in which energy is deposited into the radial component of the magnetization vector [9].

Current research on coaxial NLTLs is primarily conducted at the Center for Pulsed Power & Power Electronic (P^3E) at Texas Tech University and the Institute for High Current Electronics (IHCE) in Tomsk, Russia. Bragg provides a much more thorough discussion of the history and development of NLTLs in his doctoral dissertation [10].

1.2 Nonlinear Transmission Lines as HPM Sources

The source of the microwave oscillations in a ferrimagnetic NLTL is the damped gyromagnetic precession of magnetic moments as opposed to the oscillation of electrons as is the case for e-beam devices. The output power and frequency of the microwave oscillations is determined by the combination of material properties, the initial condition of the ferrimagnetic material, and the defining characteristics of the incident voltage pulse, e.g. rise time, amplitude, and duration.

The discussion of NLTLs must be based upon a firm understanding of micromagnetism, ferrimagnetic materials, transmission line theory, high voltage pulsers, and high voltage diagnostics. These topics will be covered in Chapter 2 before discussing the basic theory of operation and line construction methods in Chapter 3 and the experimental results in Chapter 4. An antenna to radiate the microwave power is designed and discussed in Chapter 5 as well as the experimental results of a four element linear array of NLTLs.

CHAPTER 2

BACKGROUND THEORY

The microwave oscillations seen on the output of a Nonlinear Transmission Line (NLTL) are due to the motion of magnetic moments in the ferrimagnetic material. The structure of magnetic domains have their origin at the atomic scale. The discussion of micro-magnetics will occur on a semi-classical level with the quantum derivations supplied via reference and only the relevant results presented.

Transmission line theory is discussed including a brief discussion of transient modes in a coaxial transmission line and the calculation of a characteristic impedance of a multi-dielectric line. These subjects are relevant to the theoretical discussion of NLTL operation given in Chapter 3.

An overview of high voltage pulser technologies is included to outline options for generating the incident high voltage pulse used to excite the NLTL. The limitations, and benefits of the various pulsers are outlined and discussed. Also included is a discussion of basic array theory needed to verify the experimental results given in Chapter 5.

2.1 Fundamentals of Magnetism

A magnetic field can be generated from an electric current or the intrinsic spin of an electron. Electron spin is a fundamental property of an electron analogous to charge. The electric current can refer to, an orbiting electron in an atom or the motion of the protons in the nucleus on the atomic scale, or the motion of conduction band electrons in metals on the macroscopic scale. In either case we can refer to the strength of the magnetic field in terms of a density of magnetic moments. An illustration of magnetic moment due to a current loop is shown in Figure 2.1 and the magnitude of the magnetic moment is given by Equation 2.1 where I is the current in the filamentary loop, S is the enclosed area, and μ_0 is the permeability of free space [1, 11]. For an electron orbiting an object with tangential velocity $\vec{v}$ whose position is traced out by position vector $\vec{r}$, the moment is given by Equation 2.2 [1].

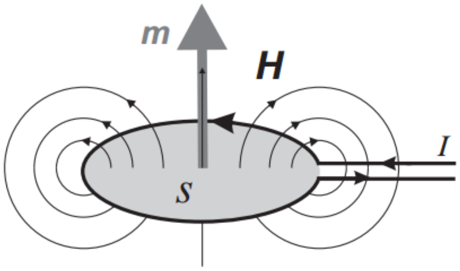

Figure 2.1: Current loop generating a magnetic moment with the magnitude proportional to the enclosed area S and current I. [1]

$$|\vec{m}| = \mu_0 IS \tag{2.1}$$

$$\vec{m} = -\frac{e\mu_0}{2}\left(\vec{r} \times \vec{v}\right) \tag{2.2}$$

Since an electron has mass an electron creating a current loop will also have an angular momentum. The angular momentum of a body is given by Equation 2.3. The cross product term is the same as seen in Equation 2.2 so we can relate the angular momentum and magnetic moment of an orbiting electron, given in Equation 2.4 [1].

$$\vec{L} = \vec{r} \times \vec{p} = m_e\left(\vec{r} \times \vec{v}\right) \tag{2.3}$$

$$\vec{m} = -\frac{e\mu_0}{2m_e}\vec{L} \tag{2.4}$$

Note the negative sign in the relation, this is due to the negative charge of the electron and means the angular momentum and magnetic momentum are anti-parallel, shown clearly in Figure 2.2. Also it is important to point out that the radius of the orbit and orbital velocity are factored out leaving a constant relation between the two quantities. This factor, with the addition of a correction factor g known as the spectroscopic splitting factor, or Landé Factor, constitutes the gyromagnetic ratio γ

given in Equation 2.5, which is negative for the case of an electron since $q = -e$ [1]. The correction factor is due to quantum effects that remove degeneracy in the energy levels of the electrons, and allow for consideration of the total angular momentum J of the magnetic ion, this effect can only be explained quantum mechanically, White [12] provides a thorough explanation.

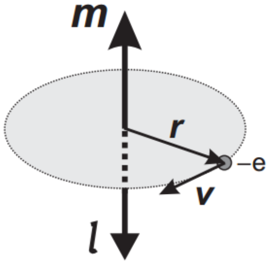

Figure 2.2: Magnetic moment and angular momentum of an orbiting electron[1]

%

$$\gamma = g\frac{q\mu_0}{2m} \tag{2.5}$$

A magnetic moment placed in an external magnetic field will attempt to align itself with the magnetic field in order to minimize energy, with the energy of a magnetic moment in an external field given by Equation 2.6. The external magnetic field exerts a torque on the moment according to Equation 2.7, and we note that torque is equal to the derivative of angular momentum [1].

$$E = -\vec{m} \cdot \vec{H} \tag{2.6}$$

$$\frac{d\vec{L}}{dt} = \vec{T} = \vec{m} \times \vec{H} \tag{2.7}$$

Taking the derivative of Equation 2.4 and substituting Equation 2.7 we obtain Equation 2.8. The result is that the motion of the magnetic moment in an external field $\vec{H}$ is to precess around the effective field with constant magnitude.

$$\frac{d\vec{m}}{dt} = -\gamma\left(\vec{m} \times \vec{H}\right) \tag{2.8}$$

2.1.1 Magnetization Dynamics

Starting from Equation 2.8 the two most familiar equations governing magnetization dynamics can be derived, the Landau-Lifshitz (LL) Equation, and the Landau-Lifshitz Gilbert (LLG) Equation. According to Equation 2.8 a moment will perpetually precess about the magnetic field $\vec{H}$ which we know is not the case, the moment will eventually align to the applied field. There must be some mechanism to dampen the precession in the direction of the magnetic field, see Figure 2.3. A damping torque is introduced that is of the correct form to account for the eventually alignment with the applied field. Landau and Lifshitz accounted for the damping by including an $\vec{M} \times (\vec{M} \times \vec{H})$ term (Equation 2.9) and Gilbert accounted for the damping using an $\vec{M} \times \frac{\partial \vec{M}}{\partial t}$ term (Equation 2.10). Both can be used at low values of the damping coefficient α, however, the behavior of the equations at high values of α are different which is discussed in Chapter 6. Note that up until Equations 2.9 and 2.10 the moments we referred to using $\vec{m}$ instead of $\vec{M}$. The capital vector $\vec{M}$ is representative of a density of magnetic moments, or magnetization of the ferrimagnetic material, while $\vec{m}$ is an individual magnetic moment. The validity of the transformation is discussed in the following section.

$$\frac{d\vec{M}}{dt} = \gamma\left[\vec{M} \times \vec{H}\right] + \frac{\alpha\gamma}{M_s}\left[\vec{M} \times \left(\vec{M} \times \vec{H}\right)\right] \tag{2.9}$$

$$\frac{d\vec{M}}{dt} = \gamma\left[\vec{M} \times \vec{H}\right] + \frac{\alpha}{M_s}\left[\vec{M} \times \frac{d\vec{M}}{dt}\right] \tag{2.10}$$

2.1.2 Application to Macroscopic Fields

The derivations given above are derived from using a single electron as an analog for any source of magnetic moment including the intrinsic spin moment of an electron in which case the electron motion is assumed to be an electron spinning on an axis

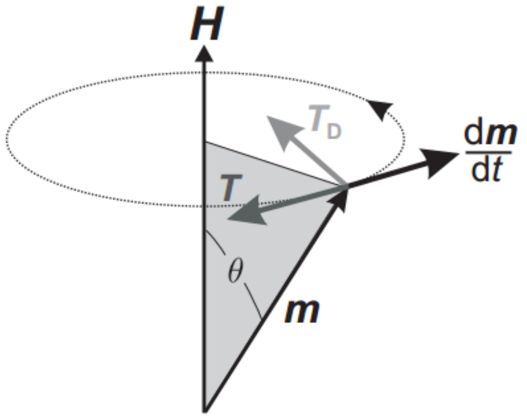

Figure 2.3: Precession of a moment around the effective field is damped by the inward direct torque T_D which forces the moment to align with the magnetic field. Inspection of vectors $\vec{\mathsf{M}}$, $\vec{\mathsf{H}}$, and $\frac{d\vec{\mathsf{M}}}{dt}$ show that both the LL and LLG equations satisfy the requirement of T_D in their damping terms. [1]

and a moment of inertia method can be employed to calculate the angular momentum and a fictitious charge density the moment. The concern is the validity of scaling this behavior to the macroscopic field levels encountered in the lab setting and dealt with in experiments conducted on NLTLs. The general validity of ignoring quantum variations when scaling to macroscopic fields is discussed in [13] and more specifically in the case of magnetic moments in [14].

When going from the single moment view of Section 2.1 to the macroscopic scale we now are talking of a density of magnetic moments and the quantity $\vec{\mathsf{m}} \rightarrow \vec{\mathsf{M}}$ where $\vec{\mathsf{M}}$ will now refer to a density of magnetic moments while $\vec{\mathsf{m}}$ is a single moment. This assumption is valid assuming a uniform magnetization over distances much greater than the distances of the interatomic spacing of the ion sites of electrons in the material in question and at temperatures much lower than the Curie Temperature T_C, that is $\mathsf{T} \ll \mathsf{T}_\mathsf{C}$ in which case the thermal agitation is not strong enough to destroy the uniform magnetization [14].

2.2 Magnetic Materials

A magnetic material is classified as diamagnetic, paramagnetic, ferromagnetic, anti-ferromagnetic, or ferrimagnetic. The two predominant factors that determine material properties are the atomic structure of the the individual elements in the material and the physical state of the material, i.e. solid, liquid, or gas. In the case of a liquid or gas the atomic structure is dominant, however, in a solid the crystal structure becomes important in determining material properties.

The distinction between paramagnetic and diamagnetic materials and so called magnetic materials (ferromagnetic, anti-ferromagnetic, ferrimagnetic) is the existence of atoms or ions in the magnetic materials that possess a net magnetic moment due to unpaired orbital or spin magnetic moments. Further distinction of magnetic materials has to due with material homogeneity and structure which affects the interaction of magnetic atoms or molecules.

An atom consists of a nucleus containing protons and neutrons and electrons that exist in orbitals around the nucleus. The electrons fill these shells in such a way as to minimize the energy of the atomic system. The location of electrons in the atom can be described by a set of quantum numbers, of which the spin quantum number $\mathfrak{m}_s$ is one, which must be unique for each electron in the system. If two electrons with different quantum numbers are at the same energy level they are said to be degenerate. In magnetic materials this degeneracy is often removed via field interactions with neighbors or external fields but these interactions are not considered here. What is important is the mechanism by which an atom can obtain an unpaired electron spin. The electrons will fill successive shells based on a set of selection rules the most important of which to consider for magnetic materials is Hund's Rule which requires that each new electron added in a given shell will have spin parallel to the other electrons in that shell until the shell is half full at which point successive electrons will have anti-parallel spin. Thus a full electron shell will have net zero spin and a partially filled shell will have a net spin [1, 2, 15]

If magnetic ions exist in an atom then the interaction of neighboring atoms will determine if the material is ferromagnetic or anti-ferromagnetic. The strength of coupling between neighboring ions in a solid can be quantified by the exchange integral J. The origin of the exchange integral is the overlap of the wave functions of nearby electrons and can be obtained using a quantum mechanical multi-electron Hamiltonian using perturbation theory, although a closed form calculation for anything but the simplest atomic system is not possible. A detailed description of exchange interactions can be found in [16, 12, 1]. Figure 2.4 shows the value of the exchange integral as a function of the interatomic distance of neighboring atoms. The sign of the exchange integral flips as the atomic distances shrink; a positive value of J will favor parallel alignment of spins while a negative value will favor anti-parallel alignment, leading to anti-ferromagnetism and ferromagnetism.

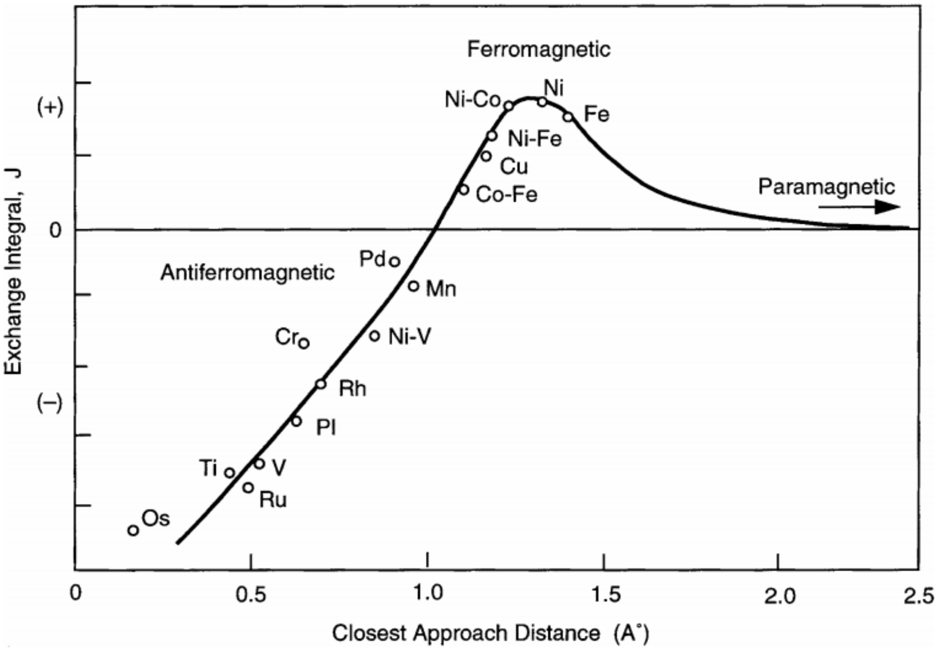

Figure 2.4: Exchange integral for different materials plotted against the interatomic spacing. Anti-ferromagnetic and ferrimagnetic material have a negative exchange integral. [2] [3]

In anti-ferromagnetic and ferrimagnetic materials more than one magnetic sub-lattices are present. In the case of different sub-lattices the material is ferrimagnetic and possesses a net magnetization M_S that is the difference of the magnetization of the sub-lattices [3, 2]. This is illustrated in Figure 2.5 which shows a relative density of interstitial sites belonging to different sub-lattices.

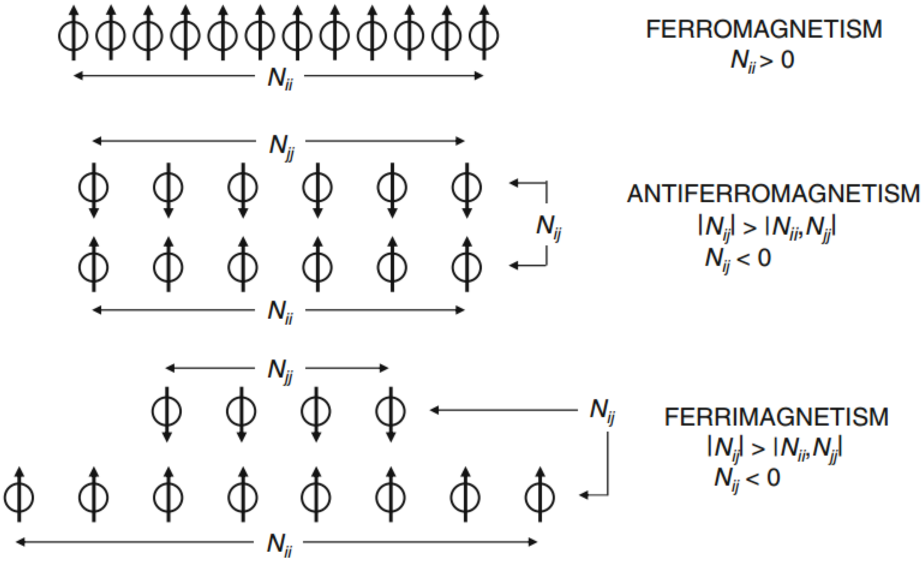

Figure 2.5: 1-D view of magnetic moments that give rise to ferromagnetism, anit-ferromagnetism, and ferrimagnetism.[2]

Ferrimagnetic substances are magnetic oxides which can contain several different magnetic ions. The cations are distributed amongst the oxygen lattices of the material. In the case of the Spinel structure these occur at tetrahedral (A sites) and octohedral (B sites) and in the case of a Garnet structure they occur at tetrahedral, octohedral, and dodecahedral sites. Three types of ferrites are used in the NLTLs: NiZn, Li, and Yttrium Iron Garnet (YIG). NiZn and Li are Spinel ferrite, shown in Figure 2.6, and YIG has a Garnet crystal structure.

2.3 Transmission Line Theory

A transmission line is a two conductor structure that guides an electromagnetic wave. The characteristics of a transmission line are determined by material properties and line dimensions. Line dimensions must be referenced to the frequencies of interest and material properties can be frequency dependent.

The characteristic impedance of a lossless coaxial transmission line is determined

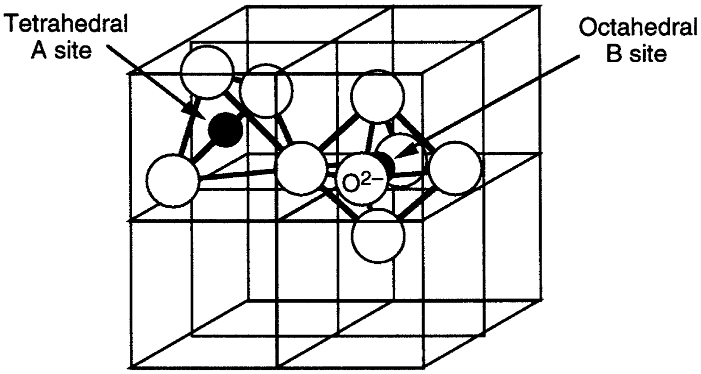

Figure 2.6: Crystal structure of a spinel ferrite showing the location of ion sites in the crystal lattice. [2]

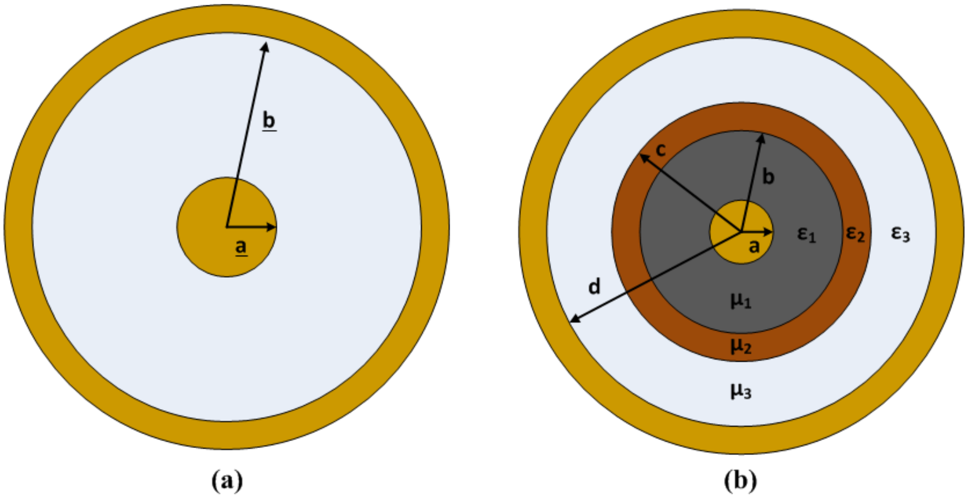

Figure 2.7: Construction of a single dielectric line (a) and a multi dielectric line (b).

by the inductance per unit length L' [H/m] and capacitance per unit length C' [F/m], given by Equation 2.11. For the case of a single dielectric line C' and L' are determined by equations Equation 2.12 and Equation 2.13 where b is the radius of the outer conductor a is the radius of the inner conductor and μ_r and $\epsilon_r$are the relative permeability and permittivity of the insulating material respectively. [11]

$$Z_0 = \sqrt{\frac{L'}{C'}} \tag{2.11}$$

$$L' = \frac{\mu_r \mu_0}{2\pi} \ln\left(\frac{b}{a}\right) \tag{2.12}$$

$$C' = 2\pi \epsilon_r \epsilon_0 \frac{1}{\ln\left(b/a\right)} \tag{2.13}$$

When the coaxial structure is made up of multiple dielectrics, as in Figure 2.7(b), Equation 2.12 is modified to an effective C' by treating each insulator as a series capacitance and Equation 2.12 is modified, in the case of a magnetic material, to account for the change in flux density due to varying μ_r. The results for the case of a triple dielectric line are Equations 2.14, 2.15, and 2.16.

$$L' = \frac{\mu_0}{2\pi} \left[\mu_1 \ln\left(\frac{b}{a}\right) + \mu_2 \ln\left(\frac{c}{b}\right) + \mu_3 \ln\left(\frac{d}{c}\right)\right] \tag{2.14}$$

$$C' = \frac{2\pi\epsilon_0}{\frac{1}{\epsilon_1}\ln\left(\frac{b}{a}\right) + \frac{1}{\epsilon_2}\ln\left(\frac{c}{b}\right) + \frac{1}{\epsilon_3}\ln\left(\frac{d}{c}\right)} \tag{2.15}$$

$$Z_0 = \frac{\eta_0}{2\pi} \left[\mu_1 \ln\left(\frac{b}{a}\right) + \mu_2 \ln\left(\frac{c}{b}\right) + \mu_3 \ln\left(\frac{d}{c}\right)\right] \left[\frac{1}{\epsilon_1}\ln\left(\frac{b}{a}\right) + \frac{1}{\epsilon_2}\ln\left(\frac{c}{b}\right) + \frac{1}{\epsilon_3}\ln\left(\frac{d}{c}\right)\right] \tag{2.16}$$

We are interested in the characteristics of a signal propagating down the transmission line and the dominant mode in a coaxial transmission line is the TEM mode. However, at high enough frequencies higher order TE and TM modes can propagate. The field lines for a TEM and TE_{11} mode are shown in Figure 2.8.

The TE_{11} mode can only propagate above a cutoff frequency f_C which is determined by the coaxial dimensions and material properties of the line. If operating below this frequency any higher order modes excited will be evanescent and can be neglected [4]. This assumption is important when describing the theory of the propagating modes excited by precessing magnetic moments in Chapter 3 and Chapter 6.

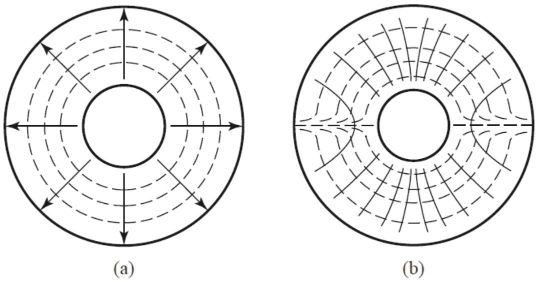

Figure 2.8: Coaxial waveguide modes (a) TEM (b) TE_{11}[4].

2.4 High Voltage Pulser Technologies

Gyromagnetic precession occurs when the moments of the ferrimagnetic material are disturbed from an initial condition and attempt to realign with an effective magnetic field. This altered effective field is provided by an incident high voltage pulse. The specifics of the system are discussed in Chapter 4 however the basic requirements of the pulser and the available technologies are discussed.

The two critical parameters when selecting a pulser are the pulse rise time and amplitude. Additionally the coaxial NLTLs are designed to have a 50 Ω characteristic impedance when saturated, therefore, the pulser must be able to supply the necessary current and store the required energy to maintain a minimum pulse width as determined by the line length and material properties. The minimum requirements will vary based on line geometry and ferrimagnetic material, however, in order to be considered as a viable source voltage amplitudes from 10 kV to 50 kV and rise-times less than 10 ns are necessary.

Solid state switches have very low jitter and are easily triggered, specifically devices such as IGBTs and MOSFETs are an obvious first choice for a high power switcher since they offer voltage controlled high current switching. Less common but more promising is a Photoconductive Semiconductor Switch (PCSS). These technologies can be used at the lower end of the operational range described above, however they can not, at this time, fulfill the requirements at the mid to high voltage ranges at which we test. For this reason a detailed discussion of solid state switches is omitted and a brief discussion of spark gaps is included.

2.4.1 Spark Gaps

A spark gap is a closing switch based on the creation of an electrical discharge Spark gaps are common in high voltage and high power applications due to the fact they can simultaneously block high voltages and switch high currents. Spark gaps can operate in either a pressurized gas environment or at vacuum; we will limit our discussion to gas gaps since they are what is used in this work.

A gap can be either triggered or operate in self-break mode. In an un-triggered gap the main gap voltage $\mathsf{V_{gap}}$ exceeds the breakdown strength of the insulating gas. A triggered gap initiates electrical breakdown by altering the gap properties, methods include distorting the electric field in the gap, changing the dielectric strength of the gap by a change in gas pressure, or providing seed electrons via a UV source as or a laser-triggered gap [5, 17].

Two types of triggered gaps are used to drive the NLTLs, a gas purge gap, and a Trigatron. A gas purge gap operates on the principle of changing the gap dielectric strength. Initially the gap is maintained at a high pressure with an increased dielectric strength relative to atmosphere, that is operating on the right hand side of the Paschen curve. Once charged to voltage the gap is vented to atmosphere reducing the gas pressure and initiating breakdown across the gap.

While the gas purge gap works well for single shot testing it is undesirable for a rep-rate operation. In order to maintain the same voltage characteristics from shot to shot, e.g. peak amplitude and rise time, the gap pressures and gas composition must remain consistent. When rep-rates in the hundreds of Hz are required the gap recovery time is too long to ensure the same gap condition for each shot. An alternative is to use an electrically triggered spark gap.

The Trigatron, shown in Figure 2.9, is a type of electrically triggered gap. A trigger electrode is located at the center of one of the main electrodes. A voltage pulse is applied to the trigger pin in either the same polarity or opposite polarity of the main gap voltage. The initiatory mechanism for breakdown can vary depending on gap configuration [18], however in the case of a heteropolarity trigger, that is the trigger pulse is of the opposite polarity of the main gap polarity, an increase in the electric field across the gap initiates breakdown.

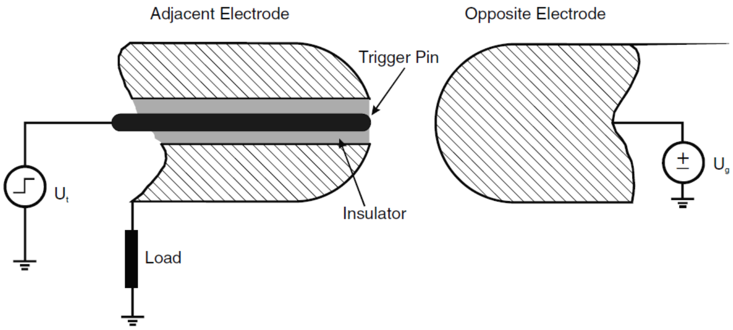

Figure 2.9: Representation of a Trigatron spark gap. The trigger electrode is pulsed initiating breakdown of the main gap [5]

Another design consideration is gap lifetime. Since a spark gap is subjected to repeated electrical discharges, electrode material can degrade over time changing gap performance. This is especially prevalent in rep-rated gaps. A few measures can be taken to increase gap lifetime. The first is proper material selection, a tougher material such as Tungsten-Carbide or Tungsten-Copper can be used to increase wear resistance. The second method is to prevent the electrical discharge from forming at the same point of the electrode, the use of a Bruce profile creates a more uniform field across the gap than a standard radius of similar dimension. In the standard radius gap (Figure 2.10(b)) there are large field enhancements localized at the corners of the gap, this is where breakdown will most commonly occur. In the Bruce profile case (Figure 2.10(a)) the high field region is distributed over a large region at the center of the gap, this is accomplished by slowly tapering the electrode away at the edges using an empirically determined sine profile [19].

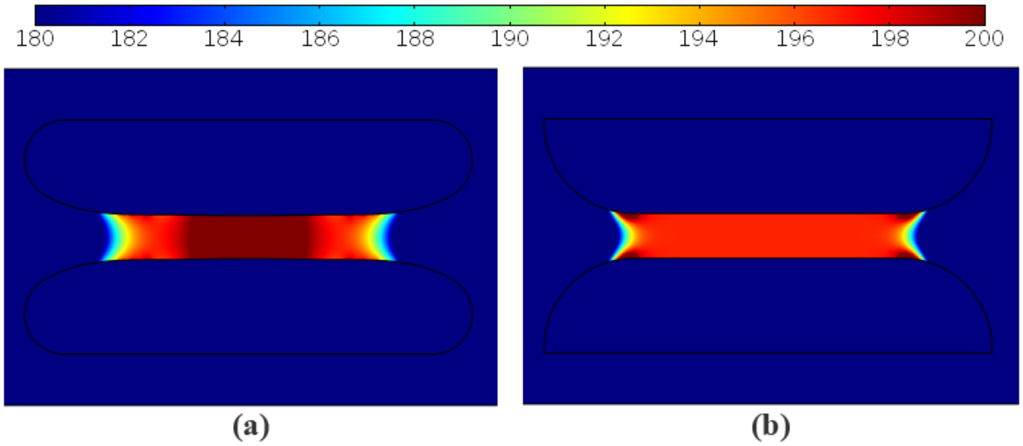

Figure 2.10: Electric Field [kV/cm] for a 2.54 mm gap with an applied voltage of - 40 kV for a Bruce Profile (a) and a simple radius transition of 5.08 mm (b). The peak field in the radius profile occurs at the transition while in the Bruce Profile it is in the center of the gap.

2.5 Antenna Arrays

In order to deliver microwave power to a target a delivery system is needed. This can be in the form of a direct feed as in the case of a transmission line and load or via a radiating element. Most HPM applications require power to be delivered to a remote target in which case an antenna is used. The output power of an NLTL is directly related to the line geometry, as will be discussed in Chapter 3 and Section 4.5 which places a limit on the output power of a single device due to voltage hold-off considerations. Therefore in order to increase radiated power on target an array of antennas can be used. An introduction to basic array theory is given to inform later discussion of array performance in Chapter 5.

An NLTL is a relatively simple and easy to construct device and therefore is ideally suited to an array. A phased array of elements allows for increase in power on target and beam steering. In the case of a transient signal, the beam steering is accomplished by introducing a time delay between elements.

The far field pattern of an array is determined by the array factor and the element factor. The array factor $A(\theta, \phi)$ is dependent on array geometry and the phase between the excitation of array elements and is calculated assuming isotropic radiating elements. The element pattern $f(\theta, \phi)$ is determined by geometry and excitation method of the individual radiating elements. The far field pattern $F(\theta, \phi)$, in cylindrical coordinates, is then given by Equation 2.17. [20, 21]

$$F(\theta, \phi) = A(\theta, \phi) f(\theta, \phi) \tag{2.17}$$

From Equation 2.17 it is apparent that since the individual element pattern is a constant, if the individual element pattern is known, a complete far field pattern can be determined by solving for a closed form solution of the array pattern. The two types of array of interest are the Uniform Linear Array (ULA) and the Uniform Circular Array (UCA) due to their simplicity.

The initial choice was the UCA, shown in Figure 2.11, due to the system geometry, as will be seen in Chapter 5. However, as seen in Figure 2.12 to recreate a scaled multi-element array, i.e. large scale arrays, at least 8 elements are needed to achieve a consistent far field pattern. The current system is designed to drive four NLTLs therefore a ULA was chosen.

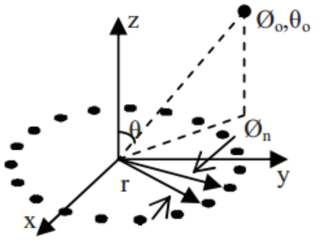

Figure 2.11: Uniform Circular Array (UCA) with equal angular spacing between elements ϕ and equal radial distance from the origin given by r. [4].

2.5.1 Uniform Linear Array

The linear array is easy to construct and reposition which makes it an ideal array for testing and verification purposes. When each element is separated by the same distance d and lies on the same plane we can refer to it as a Uniform Linear Array (ULA), shown in Figure 2.13. The ULA has a closed form solution for the array

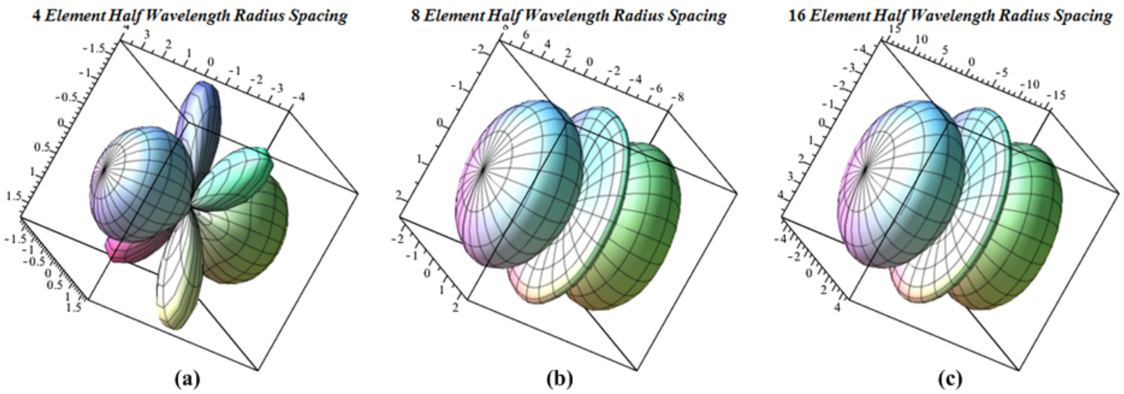

Figure 2.12: Far field radiation pattern for a 4 Element UCA (a) 8 Element UCA (b) and a 16 Element UCA (c). Once array size increase beyond 8 elements the array pattern shape in unchanged.

factor given by Equation 2.20 where θ is the angle of incidence of a plane wave, A_N is the relative excitation amplitude, β is the propagation constant, d is the element separation, and α is the relative phase of the excitation [20]. The array pattern for a uniformly excited linear array is shown in Figure 2.14.

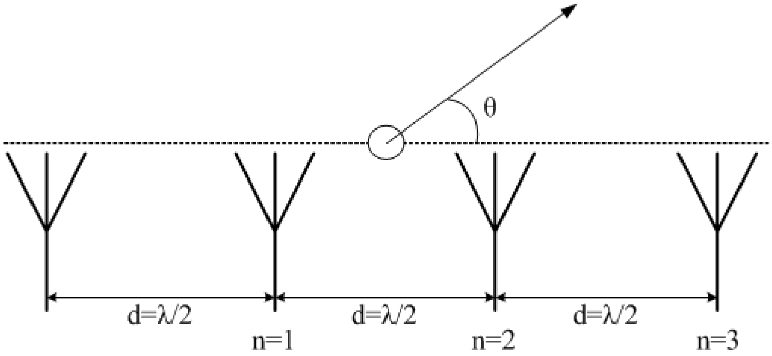

Figure 2.13: Schematic representation of a 4 element ULA with inter-element spacing of $\lambda/2$.

$$\psi = \beta d \cos(\theta) + \alpha \tag{2.18}$$

$$AF = \sum_{n=0}^{N-1} A_N e^{jn\psi} \tag{2.19}$$

$$AF = \sum_{n=0}^{N-1} A_N e^{jn(\beta d \cos(\theta) + \alpha)} \tag{2.20}$$

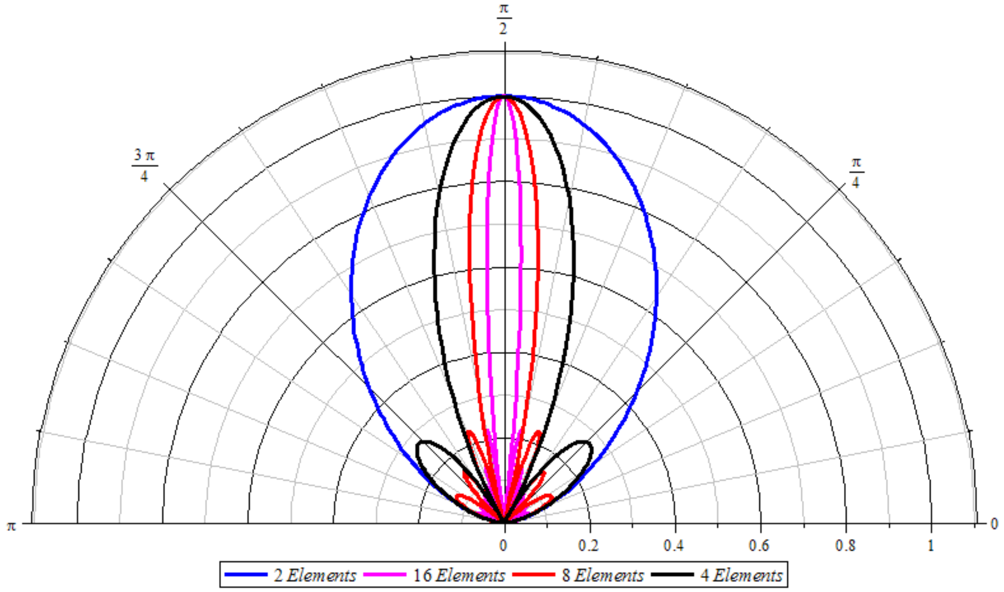

Figure 2.14: H-plane pattern of a four-element ULA with inter-element spacing of λ/2.

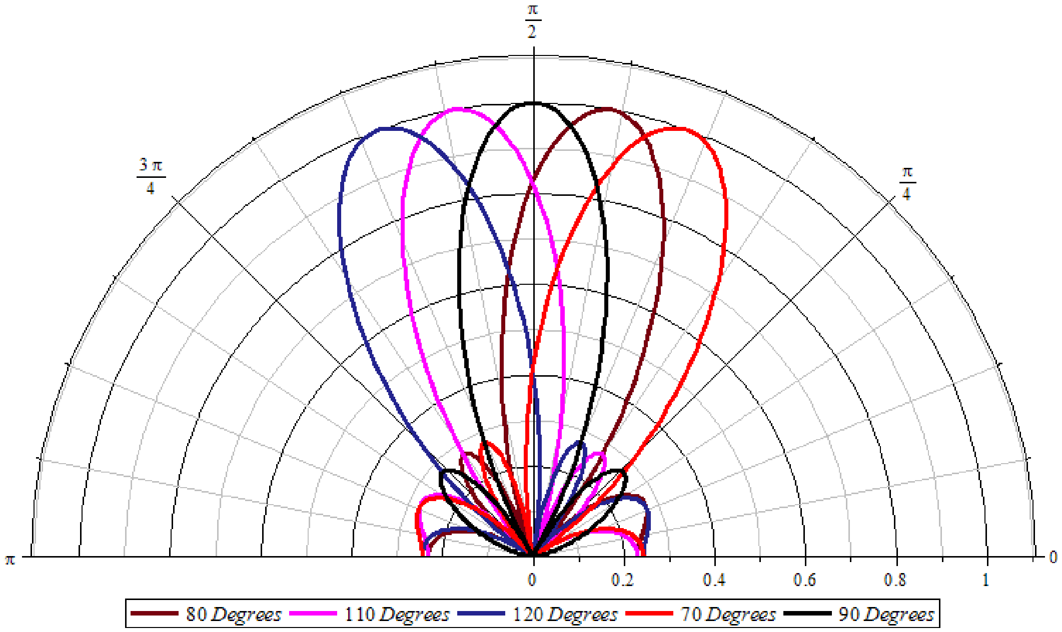

Figure 2.15: Beam steering by a four-element ULA with λ/2 inter-element spacing.

2.5.2 Far Field Region

When evaluating antenna or array performance it is important that measurements taken are in the far field region. The far-field region is the distance from the source at which the magntiude of the radiated fields exhibit a $1/r$ dependence. The conditions for far-field operation are given in Equation 2.21 where r is the radial distance from the source, D is the antenna length, and λ is the radiated wavelength [20]. For the case of a TEM Horn or aperture type antenna the parameter D is taken to be the largest antenna dimension.

$$r > \frac{2D^2}{\lambda} \qquad r \gg D \qquad r \gg \lambda \tag{2.21}$$

The TEM horn designed in Chapter 5 has a square 5" aperture therefore $D = 0.127m$. Figure 2.16 shows the distance requirements for far field operation from 1 - 8 GHz. The far field range for this aperture size is determined by the wavelength of operation, any distance over 1 m acceptable.

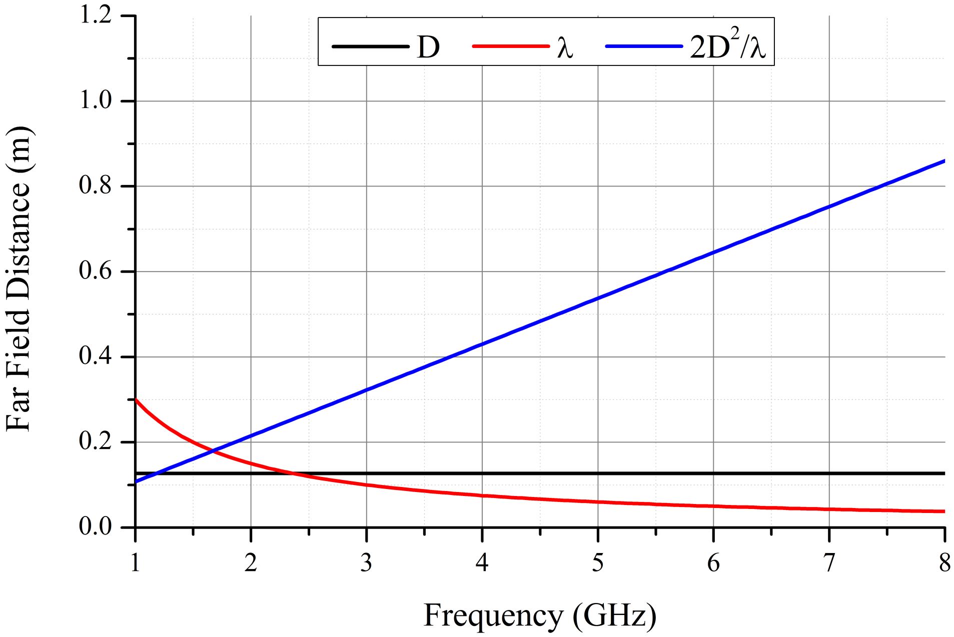

Figure 2.16: Far field distance as a function of frequency.

CHAPTER 3

BASIC THEORY OF OPERATION AND NLTL CONSTRUCTION

This chapter describes the basic theory of operation for coaxial ferrimagnetic NLTLs and describes the construction of the individual lines. The operating parameters of an NLTL are determined by the material properties and the field distribution inside the line. The line geometry, externally applied fields, ferrimagnetic material, and insulating materials, will determine the field distribution inside the line. An NLTL can therefore be designed to meet frequency and power requirements based on proper selection of ferrimagnetic material and physical construction.

3.1 NLTL Operation

An NLTL can be considered to operate in one of two modes: Pulse Sharpening Mode and Microwave Generation Mode. Coaxial gyromagnetic NLTLs produce microwave oscillations, or pulse sharpening effects, by perturbing the magnetic moments of the ferrimagnetic material. In order to maximize microwave power, coherent magnetic precession is required. Coherent precession occurs when the magnetic domains of the materials are initially of the same orientation. Figure 3.1 shows the level of magnetization in a material as a function of the applied field. The transition from pulse sharpening to microwave generation is not a clear demarcation but a gradual transition as more domains are aligned allowing enough moments to precess around a consistent effective field that a propagating TEM wave is created, and the point at which the propagating wave overcomes the losses of the line. The operating regimes of an NLTL will depend on the material properties of the ferrimagnetic material including the spontaneous magnetization $\mathsf{M_S}$, line-width $\Delta\mathsf{H}$, and loss tangent $\tan\delta$.

The magnitude and frequency of the NLTL output are related to the material properties of the ferrites, the insulating material, and the applied fields. The damping factor is related to the linewidth $\Delta\mathsf{H}$ of the ferrimagnetic material and the frequency of oscillations is determined by the effective field $\vec{\mathsf{H}}_{\mathsf{eff}}$ and the gyromagnetic ratio γ

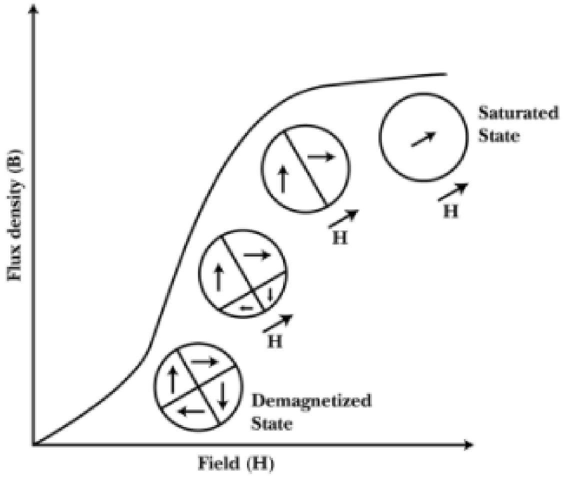

Figure 3.1: Cartoon of the level of magnetization as a function of the applied magnetic field.

according to Equation 3.1. The magnitude of the effective field will vary within the NLTL; the variation is discussed in more detail in Section 4.4 dealing with the testing of solid dielectric lines. The dimensional damping factor is related to the linewidth by Equation 3.2 where H_0 is the frequency at which ferromagnetic resonance (FMR) occurs [10].

$$\omega = \gamma \vec{\mathsf{H}}_{\mathsf{eff}} \tag{3.1}$$

$$\alpha = \frac{\Delta \mathsf{H}}{2\mathsf{H}_0} \tag{3.2}$$

3.2 NLTL Construction

Each NLTL is constructed in a coaxial geometry consisting of a metallic inner conductor, ferrites, insulating medium, and a metallic outer conductor. Two basic types of NLTL are used at Texas Tech: gas insulated and solid dielectric. Testing results are presented in Chapter 4, however, the construction of each line is discussed in the following section.

Figure 3.2 shows a relative scale size comparison of the different lines. Each line is sized to be 50 Ω to make interconnects with delay lines and diagnostics possible. Using Equation 2.16 and the material properties of the insulators and ferrites the line outer conductor is chosen to achieve as close a match as possible.

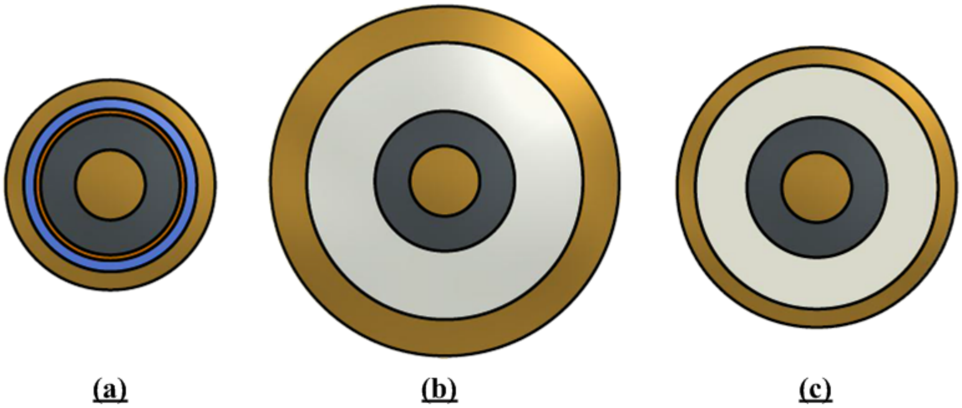

Figure 3.2: Cross Sections at relative scale of the three NLTLs constructed at Texas Tech: SF_6 Insulated Line (a), EFI Insulated Line (b), and Sylgard 184 Insulated Line (c). The size variation is due to the different dielectric constant of the insulating materials and the requirement to maintain a characteristic impedance of 50 Ω.

The ferrite inner diameter (ID) and outer diameter (OD) are constant and consequently so is the inner conductor OD. The dimensions for the lines are given in Table 3.1 and the relative permittivity and relative permeability of the material used are given in Table 3.2. When designing the line the saturated ferrite relative permeability is used so that any generated microwaves will be well matched on the output of the line. Various styles of NLTL are shown in Figure 3.3.

Table 3.1: NLTL Dimensions - Material Outer Diameter

Insulation	IC	Ferrite	Sleeve	Insulator	OC	Z_0
SF_6	3 mm	6.35 mm	6.96 mm	8.05 mm	9.53 mm	45.68Ω
Sylgard	3 mm	6.35 mm	N/A	11.07 mm	12.7 mm	50.85Ω
EFI	3 mm	6.35 mm	N/A	12.57 mm	15.88 mm	50.31Ω

In order to make the individual lines easier to connect and interchange between systems a common connector was used on all the lines. There are very few options for commercial high voltage connectors (> 20 kV) so a solution of an SF_6 filled 7/16 connector was chosen. The 7/16 connector, Figure 3.4a, is a DIN standard connector

Table 3.2: NLTL Material Properties

Material	ϵ_r	μ_r
Brass	1	1
Ferrite	3	15
Polyimide	3.5	1
SF_6	1	1
Sylgard	2.68	1
EFI	3.6	1

with readily available adapters and cable connection options and uses an air dielectric. The air dielectric feature allows the cavity to be filled with SF_6 without changing the impedance or frequency response of the connectors.

The SF_6 lines feature a polyimide sleeve, Figure 3.4b, to increase the voltage hold-off of the lines since the unity relative permittivity of the insulating material necessitates a small outer conductor to maintain a 50 Ω characteristic impedance. The small outer conductor creates a small gap between the ferrite OD and outer conductor ID.

In some cases SF_6 is required to flow through a 7/16 connector in which case custom connectors are built with holes through the dielectric spacer as seen in Figure 3.5. The custom connectors are incorporated on the entire system including the spark

Figure 3.3: Different NLTLs: from top to bottom, EFI, Sylgard, Gas fed SF_6, latest SF_6.

(a) (b)

Figure 3.4: Examples of (a) polyimide tubing and (b) standard DIN 7/16 connector

gap outputs and combiner inputs and output discussed in Chapter 4.

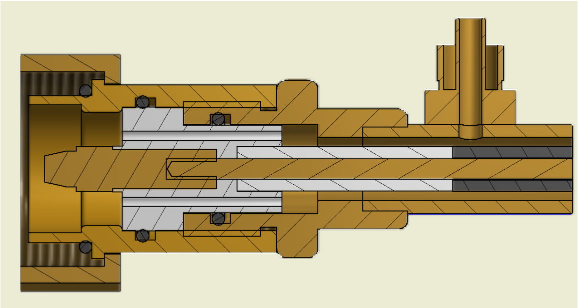

Figure 3.5: Custom 7/16 connector featuring a gas port for SF_6 in the upper right corner. The connector system fully disassembles for easy changeover of ferrites.

Figure 3.3 shows the various styles of NLTLs that have been fabricated with the SF_6 connector systems. A disassembly view of a line showing the polyimide sleeve, ferrites, inner conductor and teflon space assembly is shown in Figure 3.6.

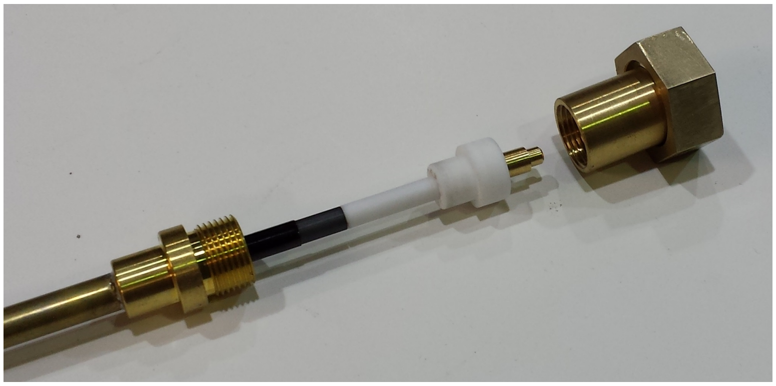

Figure 3.6: Breakdown of NLTL assembly: from left to right outer shell, polyimide sleeve, teflon spacer, IC, 7/16 housing and nut.

3.3 Ferrimagnetic Materials

Several different types of ferrite are used in the NLTLs. A commercially available NiZn ferrite from Fair-Rite and a variety of custom ferrites from Metamagnetics, Inc. Specific material values for the Metamagnetics ferrites are proprietary and will not be published, however, the relevant parameters will be discussed relative to each other and the baseline Fair-Rite product. A comparison of the materials to the Fair-Rite product is shown in Table 3.3 with $\sim$ representing similar properties, $<$ meaning a value less than and $\gg$ and $\ll$ meaning a much greater or much lower value respectively.

Table 3.3: Ferrite Materials

Material		M_S	ϵ_r	μ_i	ΔH	$\tan\delta$
FairRite	NiZn	2900	15	800	N/A	250E-6
Metamagnetics	NiZn1	$\sim$	$\sim$	$\gg$	$<$	$\sim$
Metamagnetics	NiZn2	$\sim$	$\sim$	$\gg$	$<$	$\sim$
Metamagnetics	YIG	$\ll$	$\sim$	$\ll$	$\ll$	$\sim$
Metamagnetics	Li	$\gg$	$\sim$	$\ll$	$<$	$\sim$

A much more detailed discussion of material properties, ferromagnetic resonance measurement techniques, and linewidth in particular, can be found in [10]. The materials discussed in [10] are the same materials used for testing in this work with the omission of the new Li and YIG ferrites.

CHAPTER 4

EXPERIMENTAL RESULTS

This chapter describes the experimental setups, including diagnostics used for testing of various NLTL systems and discusses experimental results. The experimental tests include:

1. Single Line
    - (a) Line Length Testing
    - (b) Ferrite Material Testing
    - (c) Solid Dielectric Evaluation
2. Dual Line
    - (a) Transient Coaxial Power Combiner
3. Multiple Lines
    - (a) Array Testing (Discussed in Chapter 5)

4.1 Spark Gaps and System Diagnostics

There are three different spark gaps used to drive the NLTL systems: a single output gap (SingleLine Gap), a dual output gap (Dual Gap), and a four output gap (MultiLine Gap).

The SingleLine gap is a pressurized gas purge operated single shot gap used to test individual NLTLs. The electrodes are 0.5 inches in diameter with gas fed in from the negative HV electrode. The negative electrode can be adjusted to operate at various voltages ranging from 10 kV - 50 kV usually operated with 2-4 nF of capacitance.

The Dual Gap is designed to drive two NLTLs simultaneously. The gap can be operated using the gas purge method of the SingleLine Gap or triggered. A trigatron is built into the output electrode of the gap allowing for triggered rep rate operation.

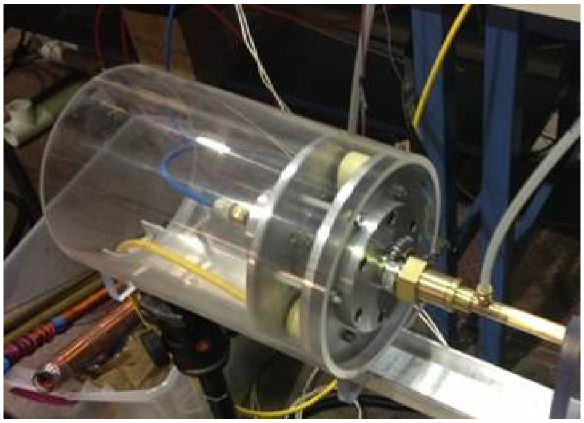

Figure 4.1: SingleLine spark gap

The electrodes are 1 inch in diameter and are made of 80:20 Copper Tungsten with a Bruce profile, see Figure 2.10. The negative HV electrode features a micrometer adjustment stage for adjustment of the gap for varied voltage operation.

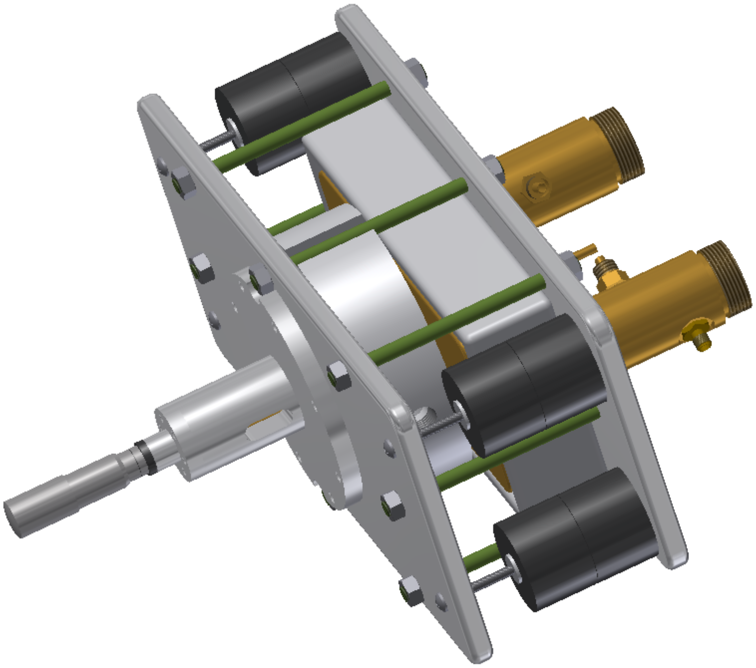

Figure 4.2: Dual spark gap

The MultiLine gap, Figure 4.3 is a four output gas purge gap featuring the same adjustable electrode setup as the SingleLine gap. The output electrode is connected to a distribution plate which splits into the four NLTL outputs via 7/16 connectors.

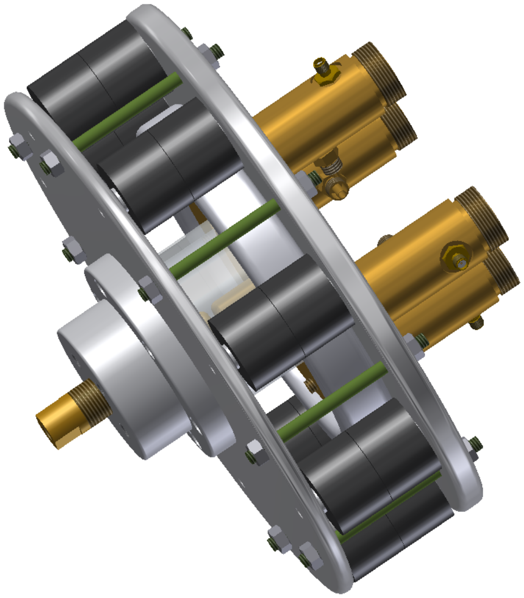

Figure 4.3: MultiLine spark gap

The system diagnostics consist of Capacitive Voltage Probes (CVP). The CVP is capacitively coupled to the inner conductor of the coaxial structure and provides a minimally intrusive way of measuring voltage. Three different probes are used on the system, one style on the output of the spark gaps, one style on the input of the combiner, and one style designed to be used on LMR-600 microwave cable. The CVPs are shown in Figure 4.4. Each probe consists of a copper patch separated from the outer shield of the coax by a 10 mil polyimide sheet with an SMA connector soldered to the patch. Depending on the values of the CVP capacitances and resistance the response of the CVP will either see the derivative of the signal, or be self-integrating. The calibration of the probes is supplied in Appendix 7.

4.2 Line Length Testing

Very little literature exists concerning the minimum line length required to generate microwaves from a coaxial NLTL. Dolan was able to fit experimental results of pulse sharpening in coaxial NLTL to a calculation of the flux swing caused by a given incident voltage and derive an approximate minimum line length.

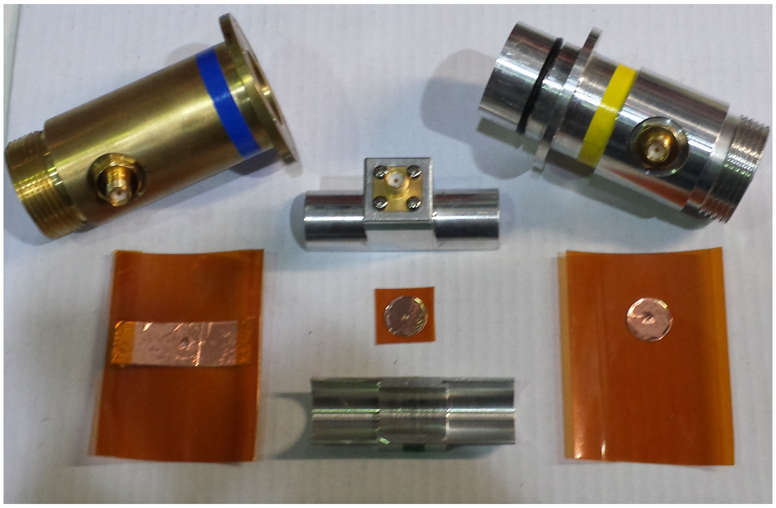

Figure 4.4: Types of Capacitive Voltage Probes (CVP) used in the experimental setup. From left two right: Spark Gap Output Probe (GAP), LMR-600 probe (LMR), and Combiner Input Probe (CMB).

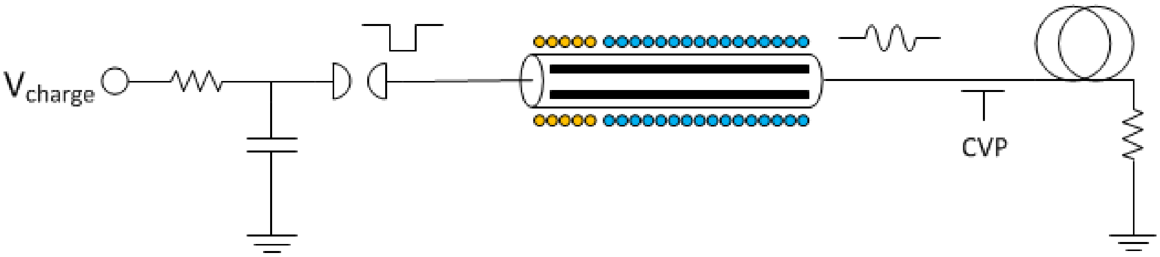

Figure 4.5: Schematic of the single line test setup used for line length testing and material testing

Several lengths of NLTLs were tested to determine the minimum length for microwave generation from 15.24 cm to 76.2 cm in 7.62 cm increments. Each line was tested using the SingleLine gap with a 20 ns delay line. Each line length tested used MX7 ferrites and was fully biased. The bias field was swept from 15 kA/m to 35 kA/m at charge voltage of 20 kV, 25 kV, 30 kV, 35 kV, and 40 kV. Three shots were performed at each combination of charge voltage and bias. A picture of the various lines in shown in Figure 4.6 and the results are presented in Figures 4.7 - 4.20. Inspection of the above mentioned figures shows three general trends; an increase in peak-to-peak voltage with increased charge voltage, a decrease in center frequency with an increase in charge voltage, and an increase in frequency with increased bias

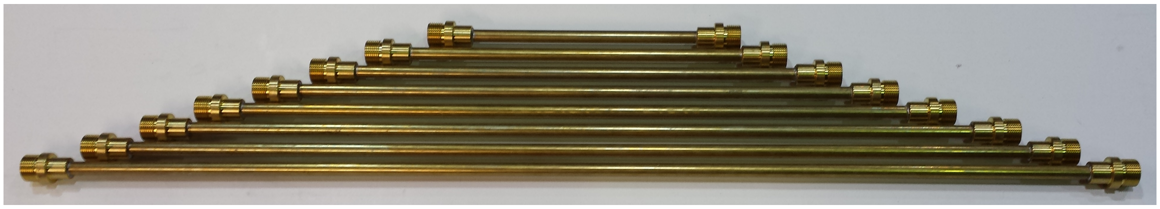

Figure 4.6: Different length shells used for line length testing

field. Peak-to-peak voltages increase with increasing bias field until the ferrites are saturated at which point further increase in bias field results in a lower peak voltage. This is due to the fact that increasing in the axial bias field results in an increase $\vec{z}$ component of the effective magnetic field $\vec{\mathsf{H}}_{\mathsf{eff}}$ resulting in the moments precessing around an effective field that is more closely aligned to $\vec{z}$ and less aligned with $\vec{\phi}$. The component of the magnetization along $\vec{\phi}$ is the signal that propagates down the NLTL.

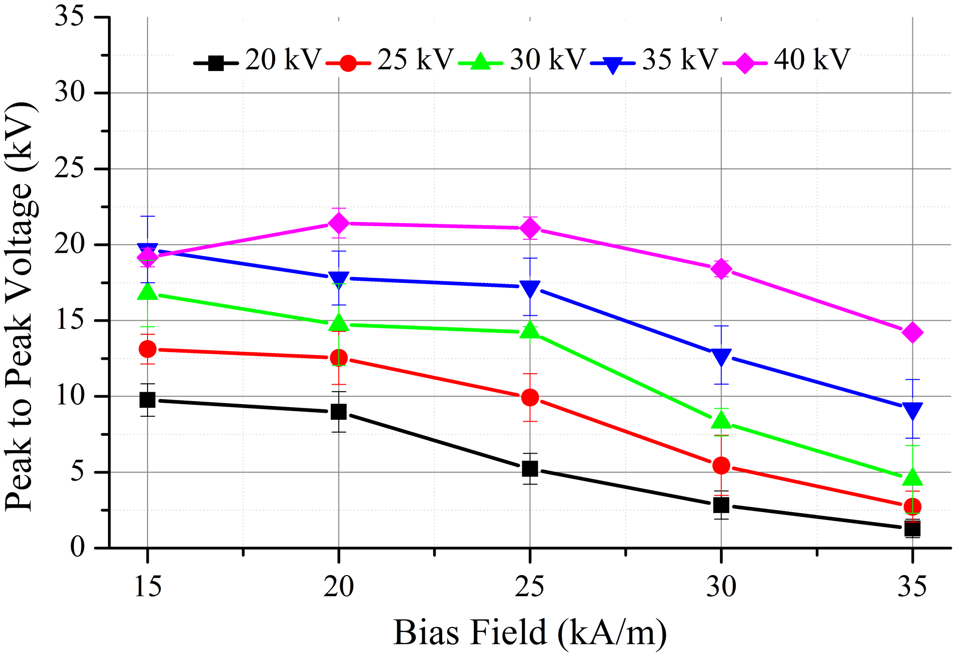

Figure 4.7: Peak to Peak voltage as a function of bias field from 20 kV - 40 kV - 9" Line

An example series of waveforms is plotted for a bias field of 20 kA/m, which is on average the best performing bias, and charge voltage of 30 kV, in Figure 4.22. The waveforms appear to show a decrease in power but what is observed is a loss of the

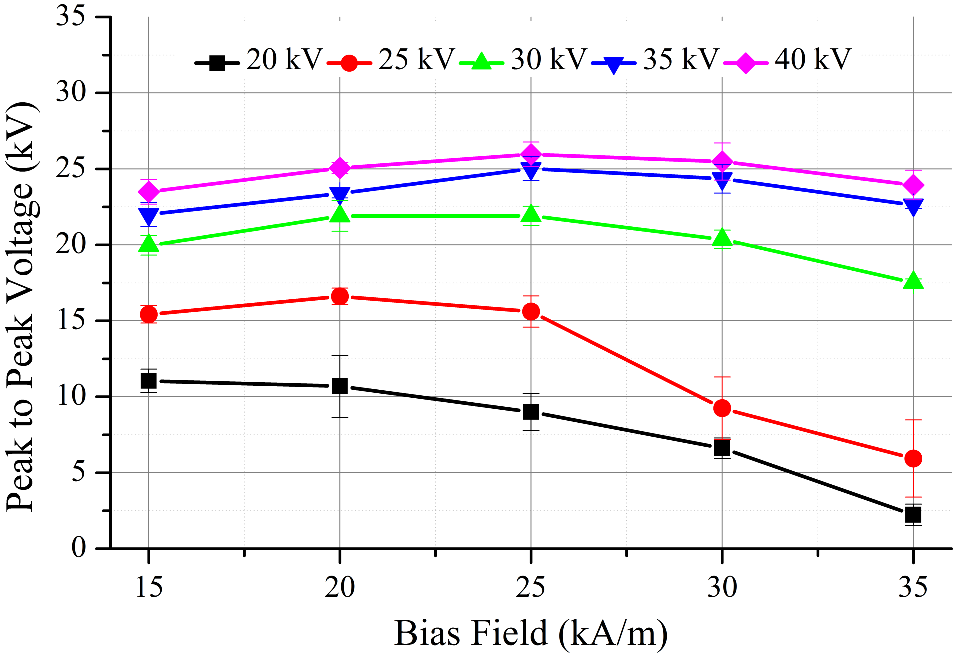

Figure 4.8: Peak to Peak voltage as a function of bias field from 20 kV - 40 kV - 12" Line

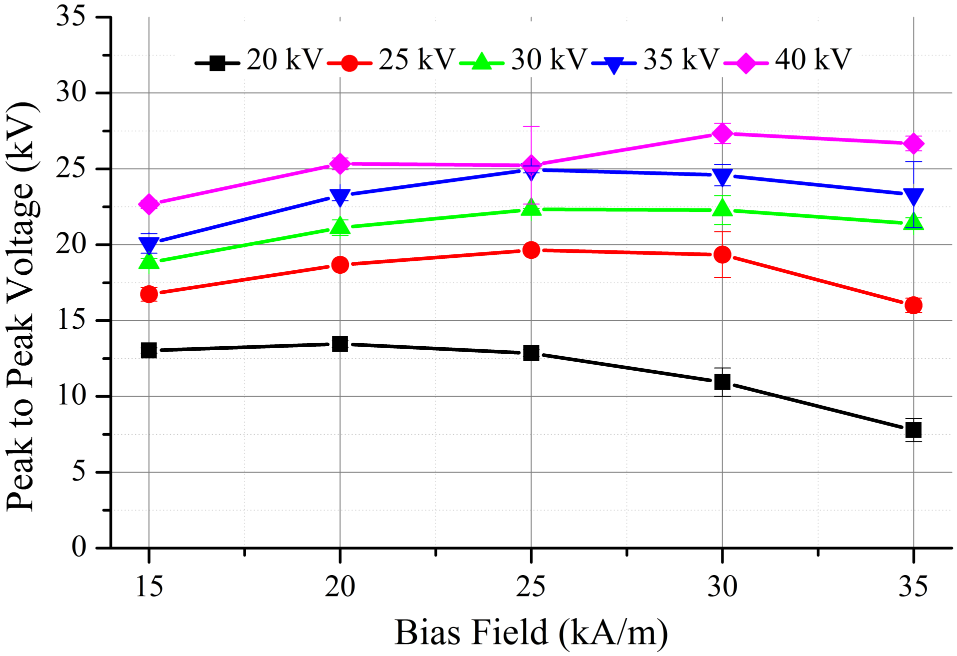

Figure 4.9: Peak to Peak voltage as a function of bias field from 20 kV - 40 kV - 13" Line

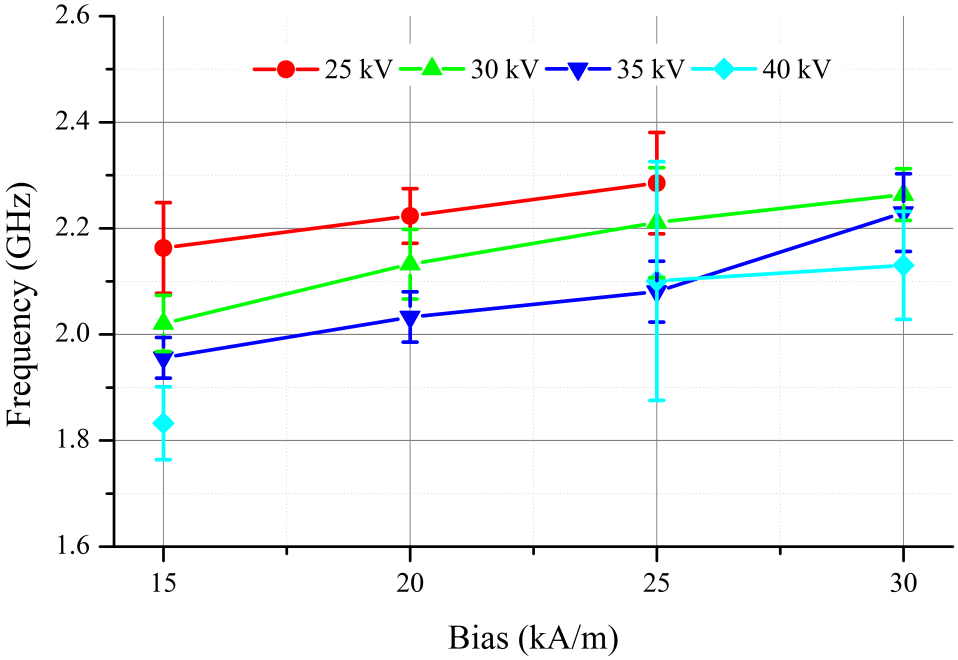

Figure 4.10: Center frequency as a function of bias field from 25 kV to 40 kV - 15” Line

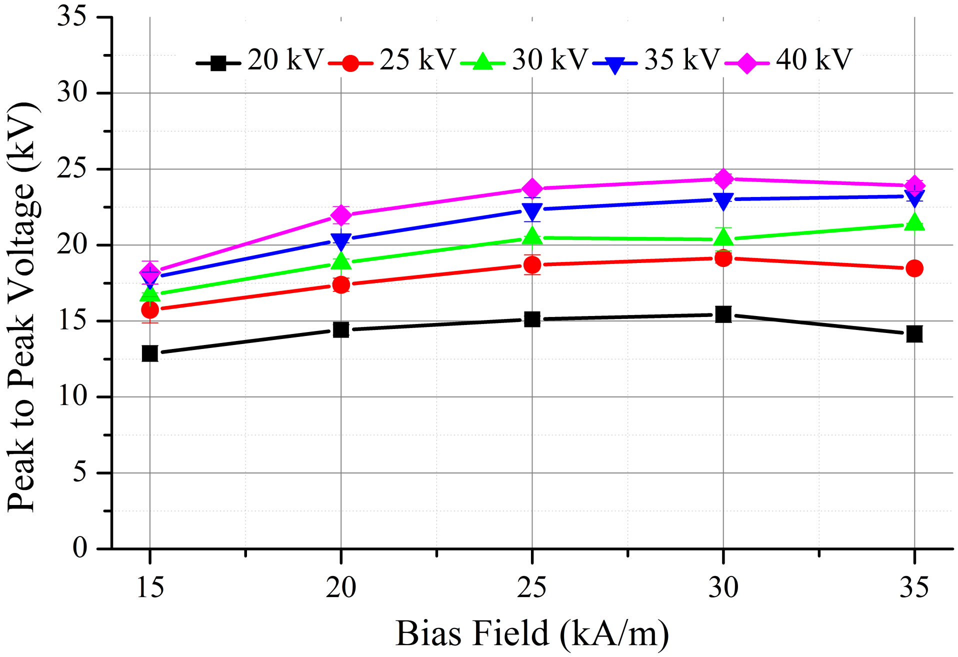

Figure 4.11: Peak to Peak voltage as a function of bias field from 20 kV - 40 kV - 18” Line

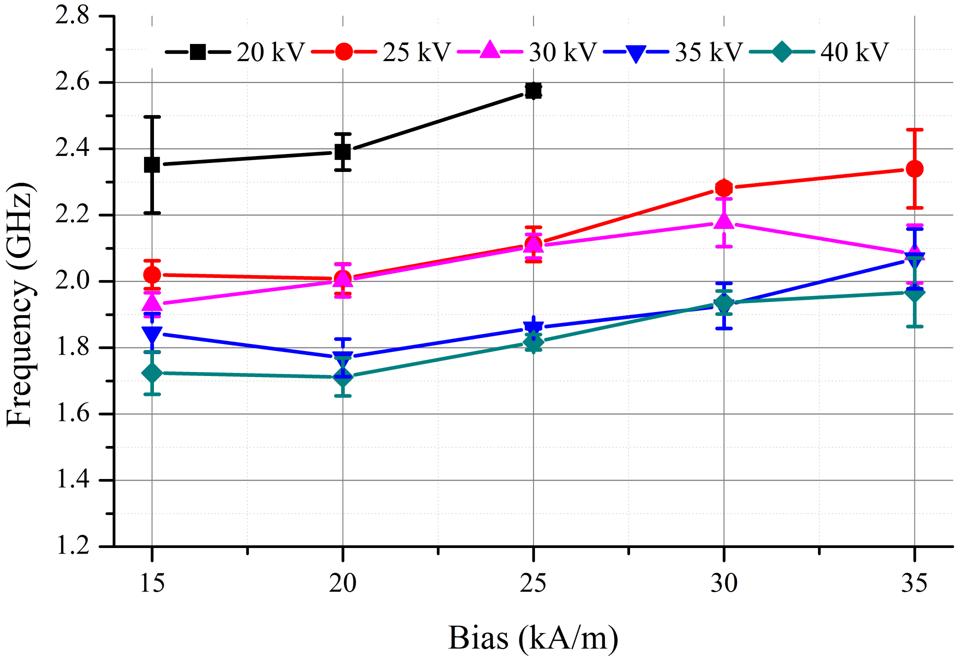

Figure 4.12: Center frequency as a function of bias field from 20 kV to 40 kV - 18" Line

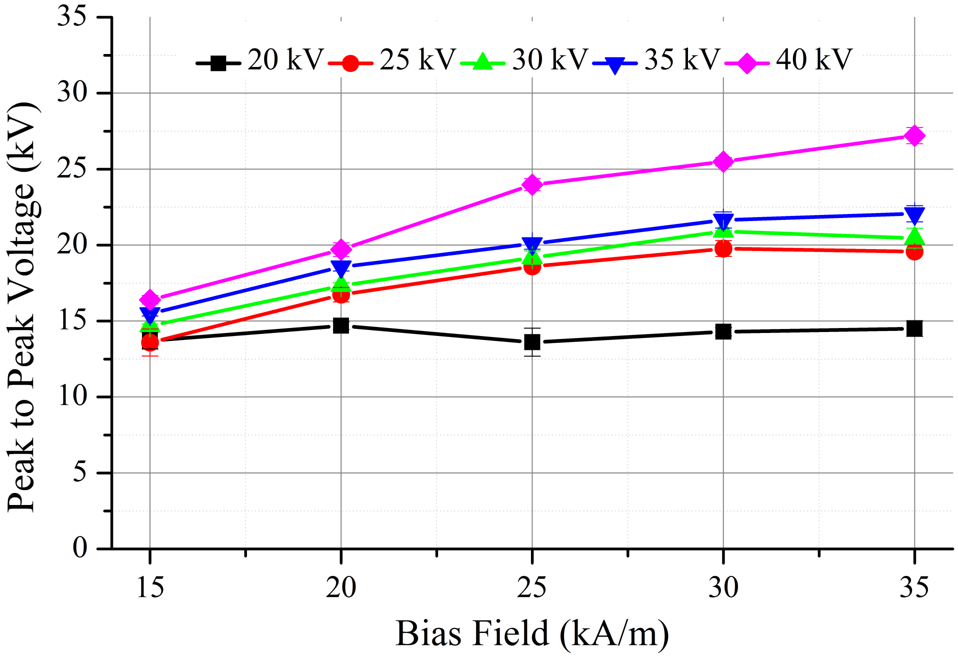

Figure 4.13: Peak to Peak voltage as a function of bias field from 20 kV to 40 kV - 21" Line

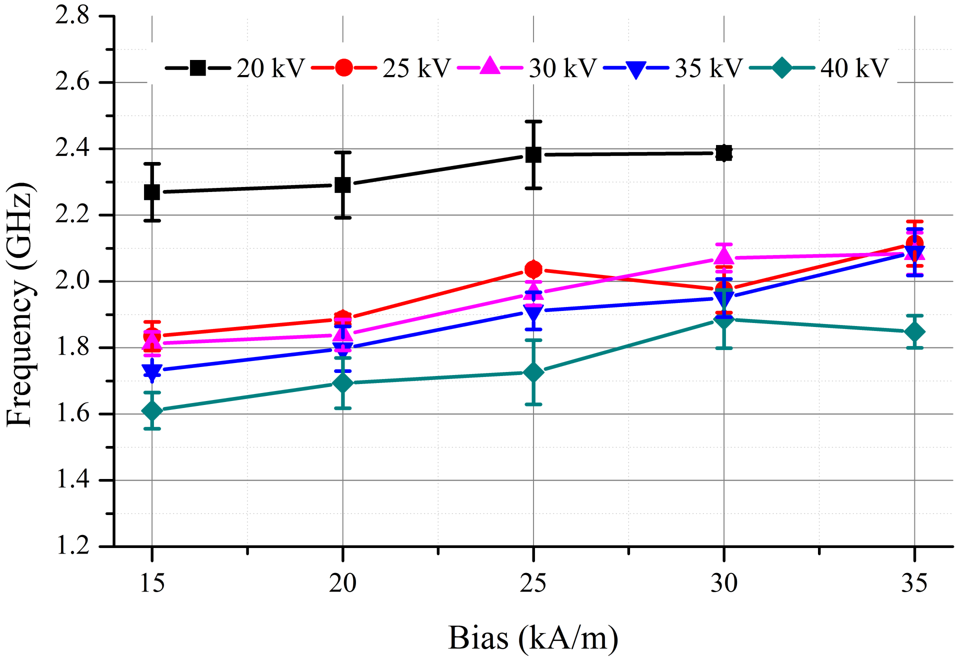

Figure 4.14: Center frequency as a function of bias field from 20 kV to 40 kV - 21" Line

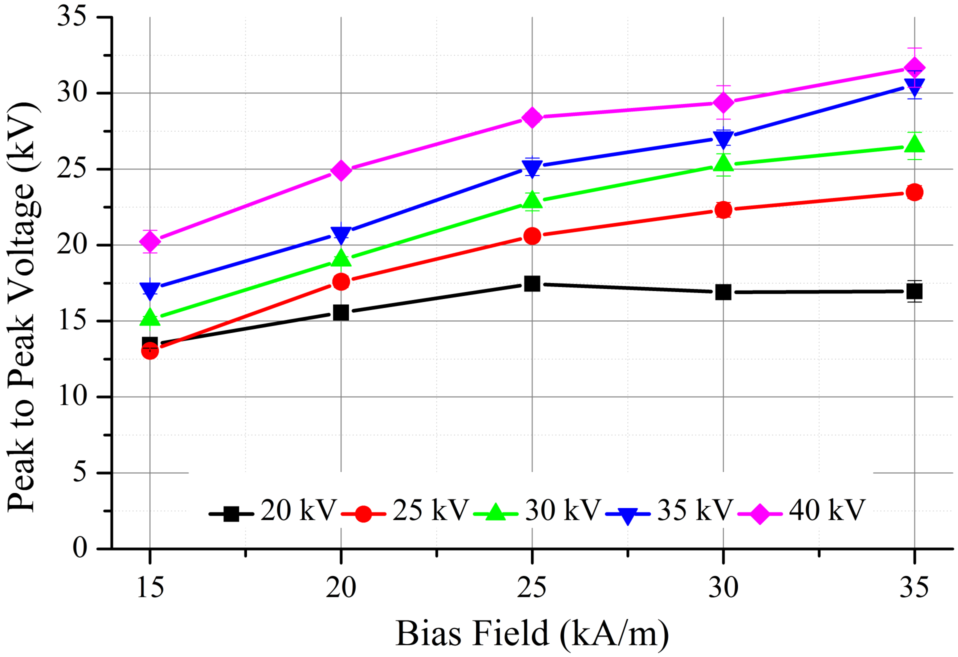

Figure 4.15: Peak to Peak voltage as a function of bias field from 20 kV to 40 kV - 24" Line

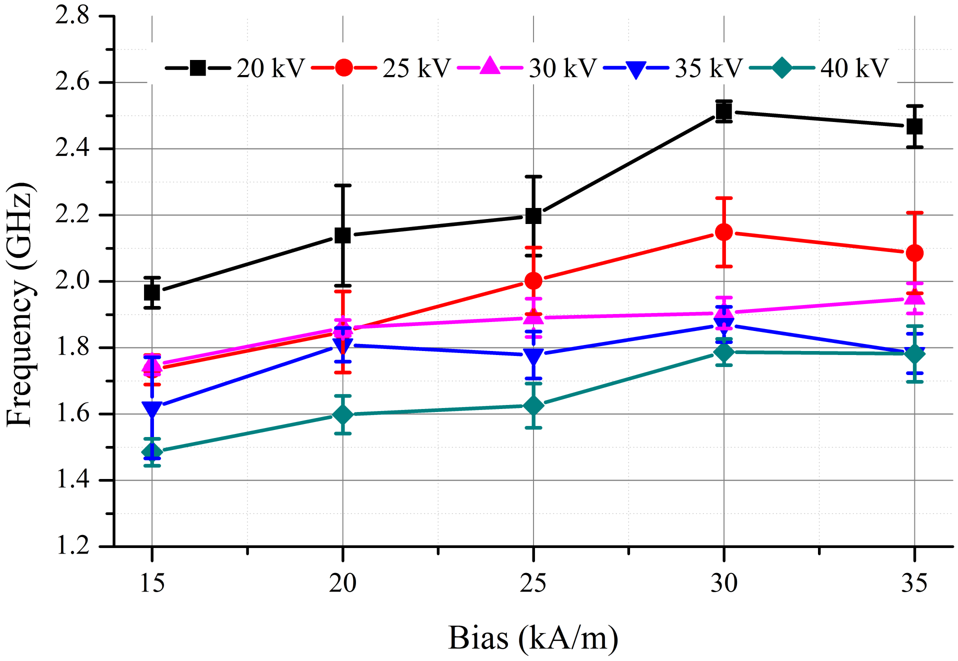

Figure 4.16: Center frequency as a function of bias field from 20 kV to 40 kV - 24” Line

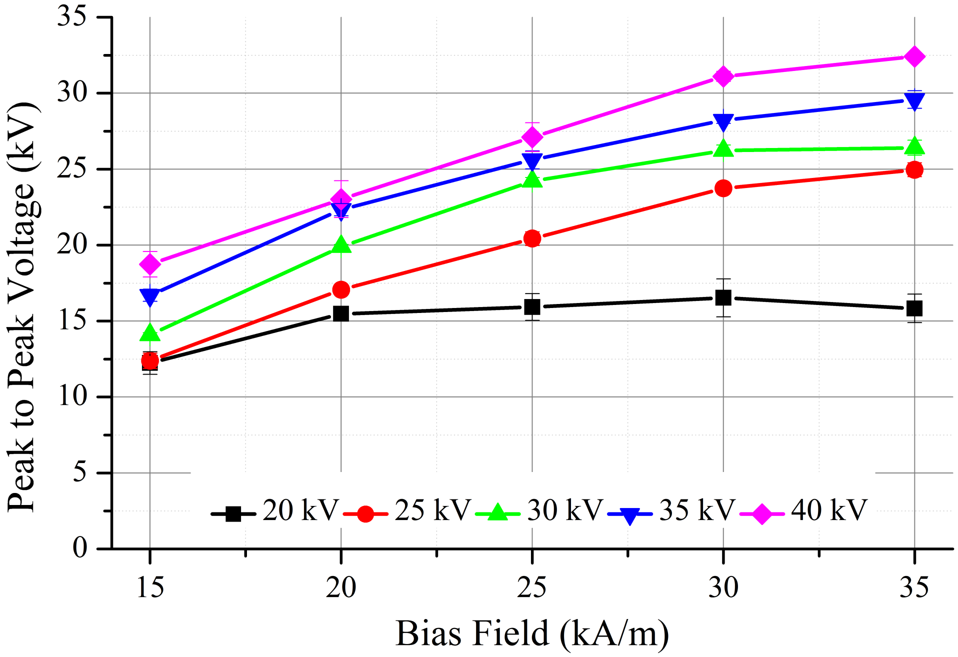

Figure 4.17: Peak to Peak voltage as a function of bias field from 20 kV to 40 kV - 27” Line

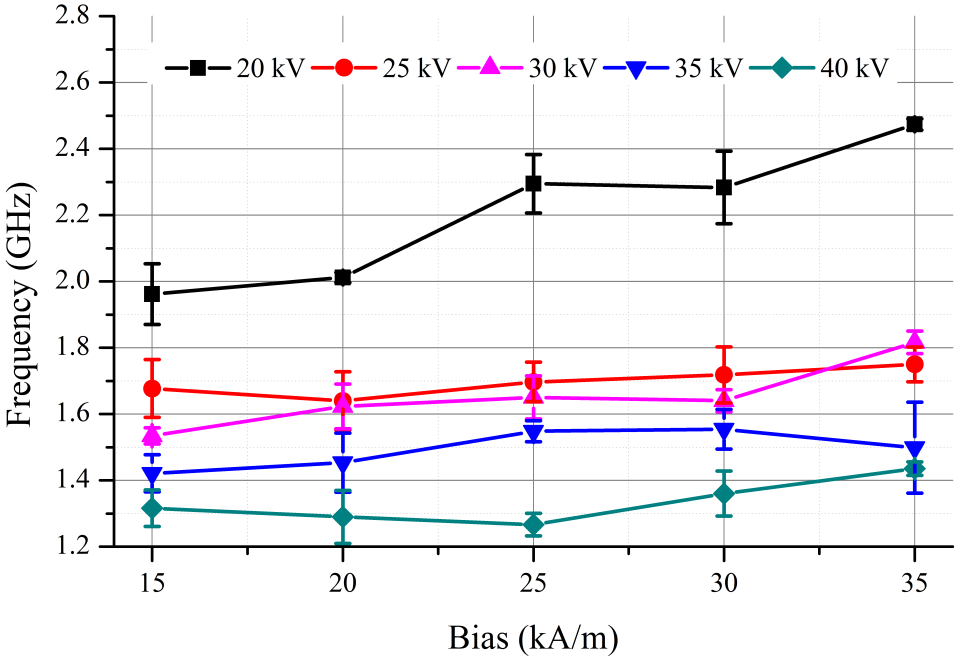

Figure 4.18: Center frequency as a function of bias field from 20 kV to 40 kV - 27” Line

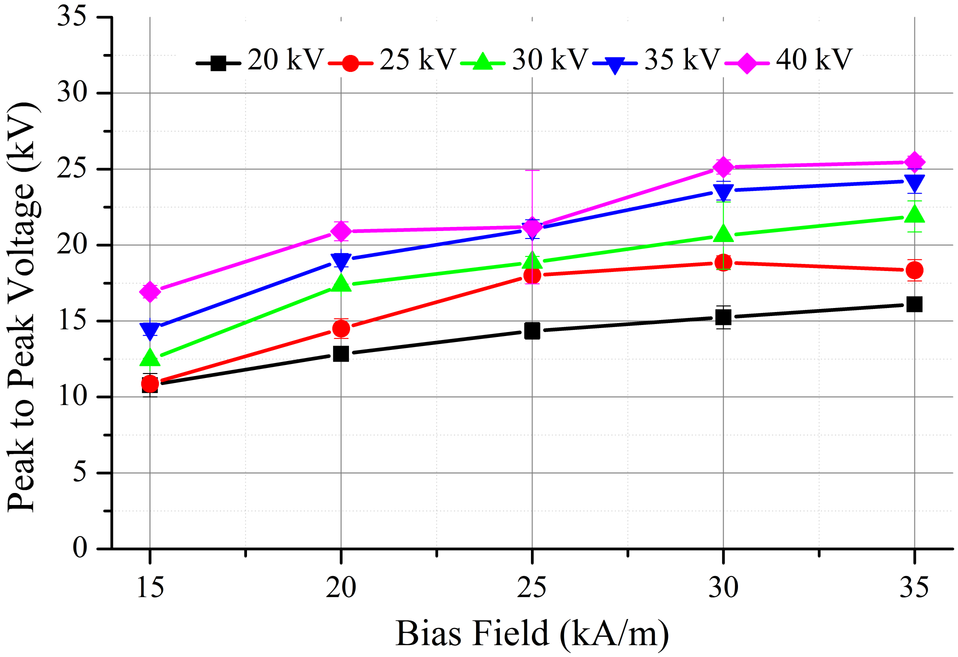

Figure 4.19: Peak to Peak voltage as a function of bias field from 20 kV to 40 kV - 30” Line

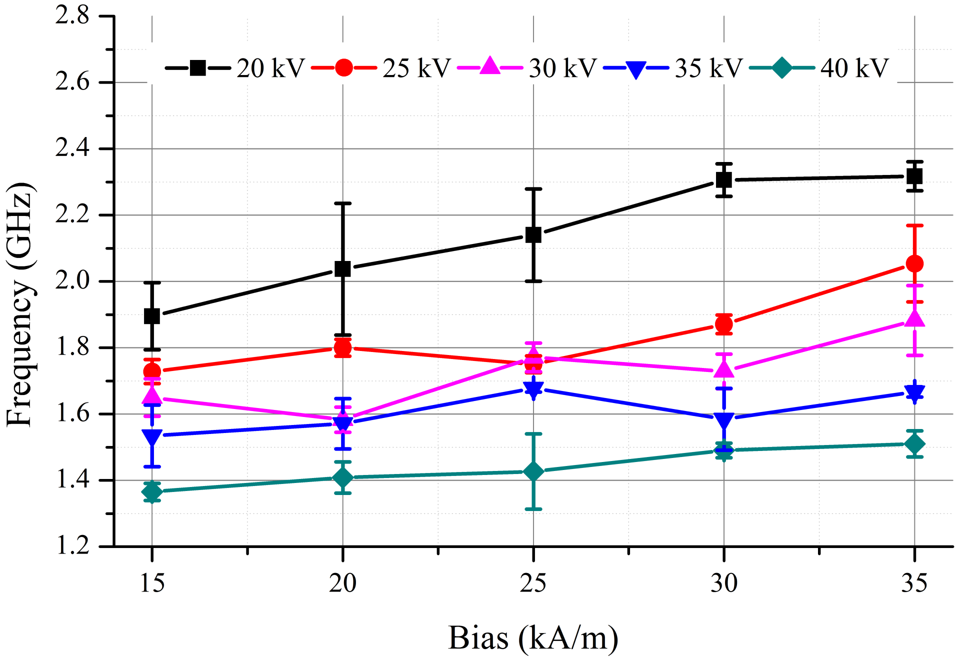

Figure 4.20: Center frequency as a function of bias field from 20 kV to 40 kV - 30" Line

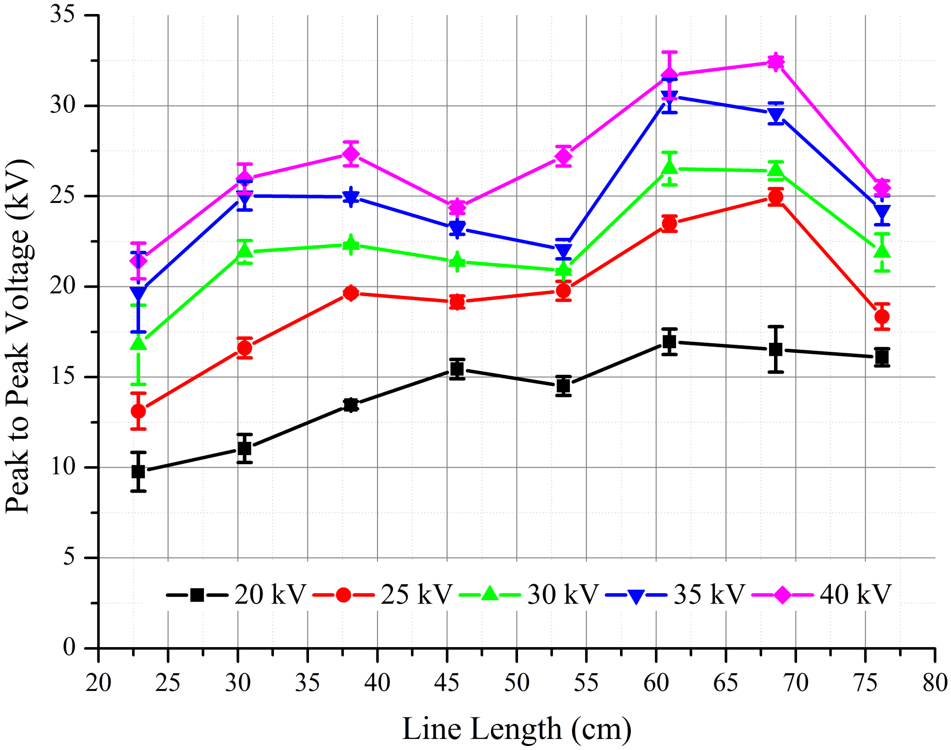

Figure 4.21: 9 Inch Line Length Testing.

dc offset of the pulse. The peak to peak voltage, measured from the first negative peak to the next peak, increases with line length up to 27 inches as can be seen from Figure 4.21.

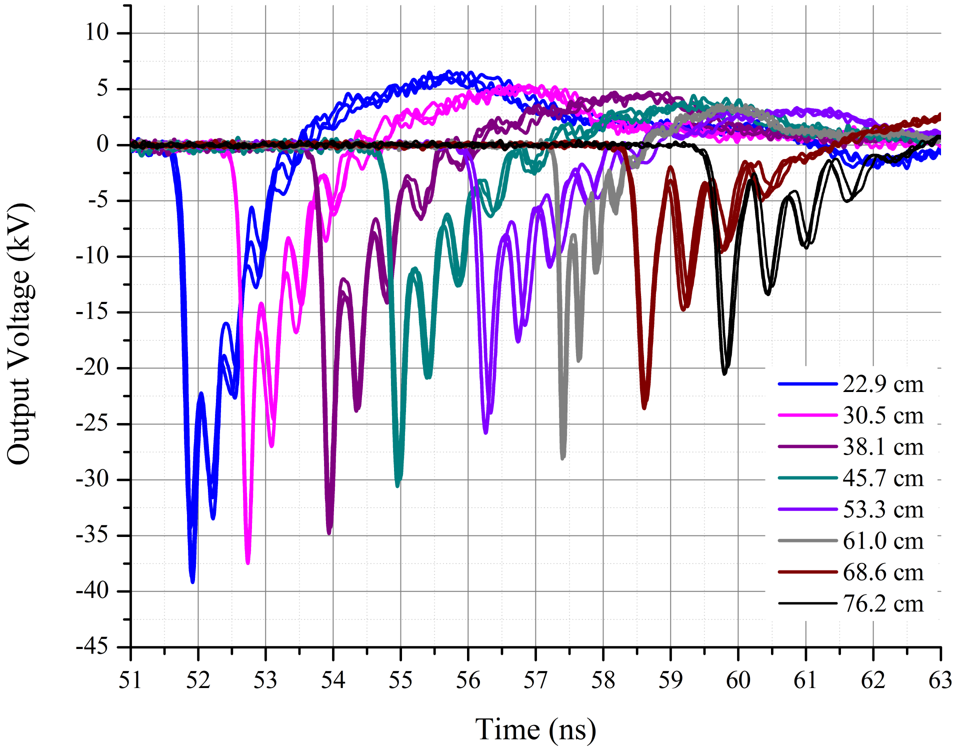

Figure 4.22: Waveforms of three shots at each line length at 30 kV and 20 kA/m bias. Waveforms are shifted in postprocessing.

4.3 Ferrite Material Testing

Earlier testing compared commercial NiZn ferrites to proprietary NiZn based ferrites from MetaMagnetics [22, 10, 23]. In addition to the MX5, MX7, and MX8 ferrites previously tested, samples of the Li ferrites and YIG ferrites discussed in Section 3.3 were tested using the SingleLine gap test setup. All material comparison waveforms and data were tested using the 76.2 cm line for a consistent comparison.

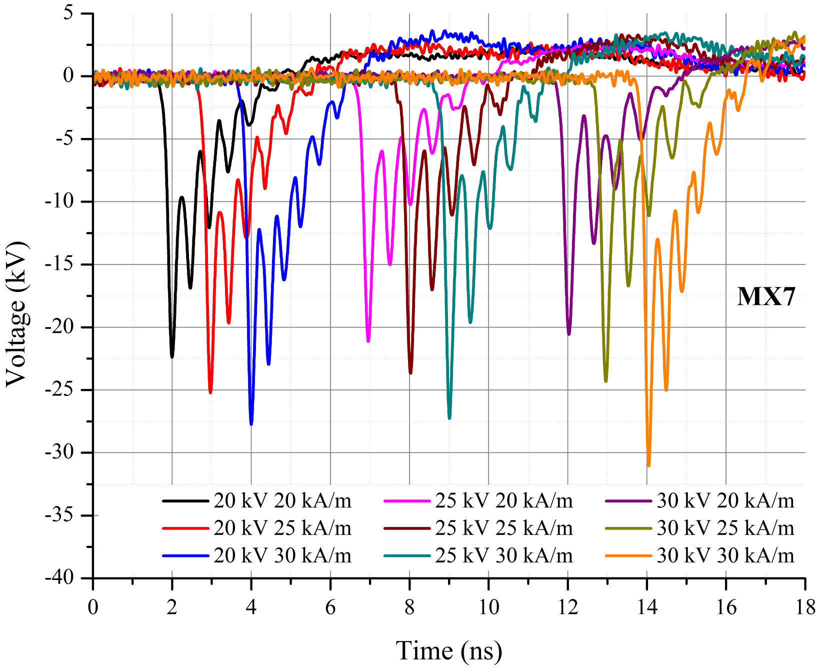

Figure 4.23: Waveforms of MX7 ferrite testing with charge voltages of 20 kV, 25 kV, and 30 kV with bias fields ranging from 20 kA/m to 30 kA/m.

The Lithium ferrites did not perform as well, in terms of both peak voltages and number of oscillations, as the previously tested NiZn or YIG ferrites at the usual charge voltages and biases. However, as seen in Figure 4.26 at 20 kV charge voltage the Li ferrite is showing an increase in peak voltage and oscillation strength as the bias field is increased. Testing was stopped at 30 kA/m bias due to the voltage limit of our dc charging supply and the bias coil resistance. It is expected that this upward trend will continue as the bias field is increased and the Li ferrite requires further testing.

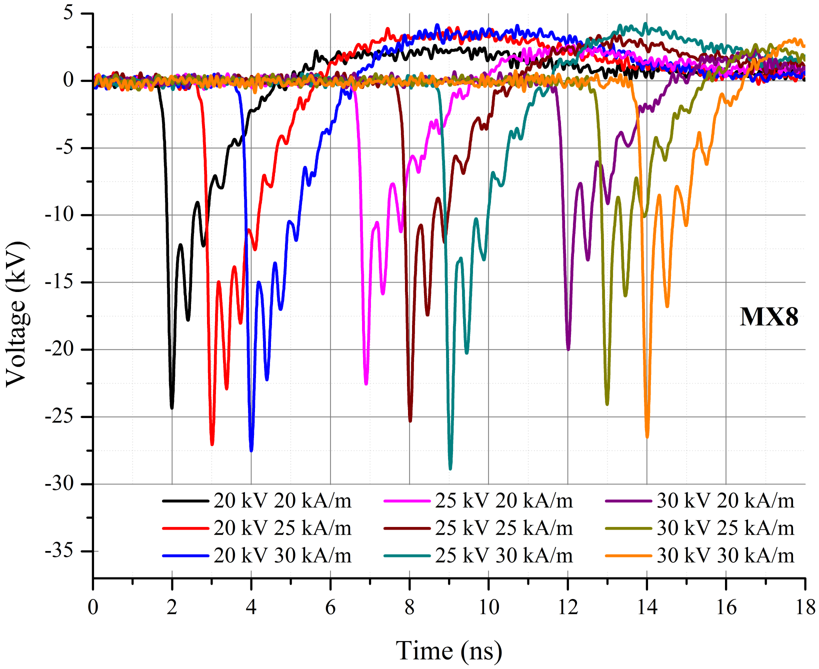

Figure 4.24: Waveforms of MX8 ferrite testing with charge voltages of 20 kV, 25 kV, and 30 kV with bias fields ranging from 20 kA/m to 30 kA/m.

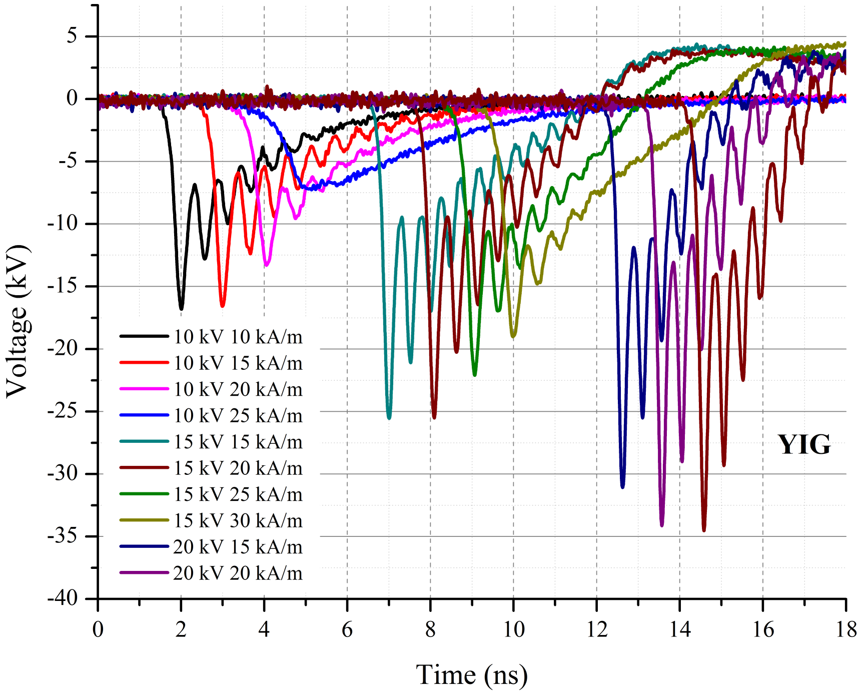

Figure 4.25: Waveforms of YIG ferrite testing with charge voltages of 10 kV, 15 kV, and 20 kV with bias fields ranging from 10 kA/m to 30 kA/m.

Table 4.1: Ferrite Material Results

Material	Charge	Bias	Peak Voltage	Peak Power	Frequency
Material	(kV)	(kA/m)	(kV)	(MW)	(GHz)
MX7	20	30	15.65	4.90	2.27
MX7	30	30	19.21	7.38	1.89
MX7	40	25	19.06	7.27	1.75
MX8	20	30	12.61	3.18	2.56
MX8	30	30	15.79	4.99	2.37
MX8	40	30	18.04	6.51	2.04
YIG	10	15	10.67	2.28	1.56
YIG	15	20	16.02	5.13	1.85
YIG	20	20	21.22	9.01	2.08

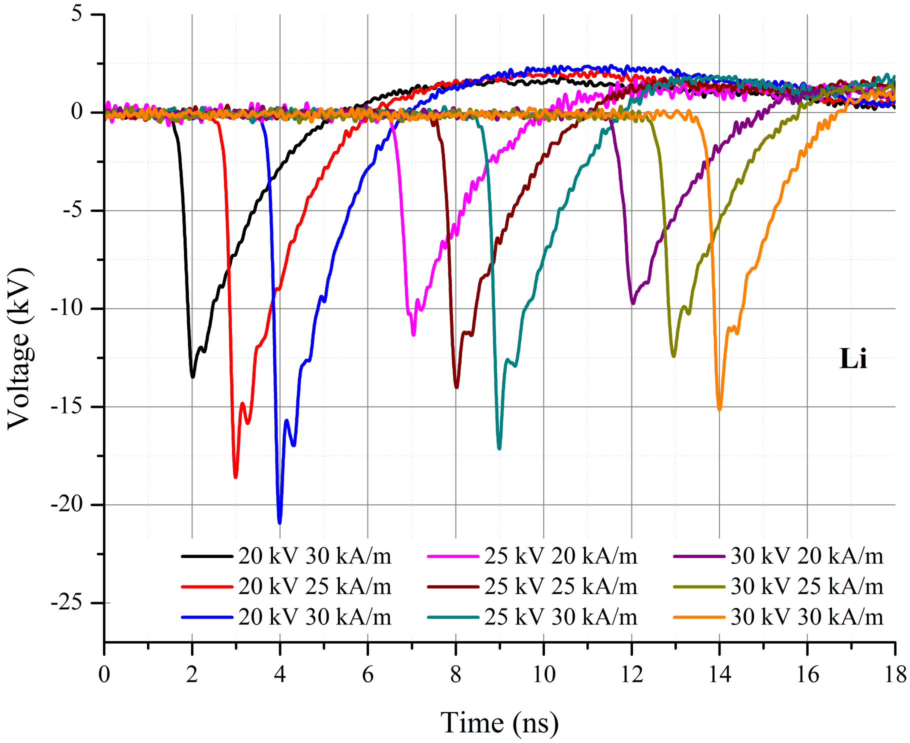

Figure 4.26: Waveforms of Li ferrite testing with charge voltages of 20 kV, 25 kV, and 30 kV with bias fields ranging from 20 kA/m to 30 kA/m.

4.4 Solid Dielectric Testing

Previously all NLTLs tested at Texas Tech have used pressurized SF_6 as an insulator. This was for several reasons: ease of construction, recovery from breakdown events, and easy change out of magnetic materials. However there are drawbacks including the cost of SF_6 and the requirement to store a volume of compressed gas near your system. Vacuum oil has also been used, most notably in the systems used by Romanchenko at IHCE in Tomsk [24].

The desire was for a solid dielectric insulator. The solid dielectric would have to have an adequate dielectric strength and a low loss tangent. Initial research into pre-fabricated solid dielectrics were not fruitful; either it was too difficult to bore out very long solid materials at the lengths required for the NLTL or extruded tubes had non-uniformities and voids that lead to triple points and breakdown in the line. It was determined that a potting material was required.

Two options were suggested EFI 50013 20002 (EFI) and Sylgard 184 (Sylgard). There was very little data on the loss tangent of EFI and what was provided was measured at very low frequencies. The losses of EFI even at the low frequencies were alarmingly high and thus Sylgard was chosen as a second option since it had an order of magnitude lower loss tangent. In order to evaluate the materials sample lengths of 0.25 inch diameter material were cast to test in a cavity resonator. The results are given in Table 4.2. A piece of Rexolite 1422 was used as a control since it had published data on the loss tangent at the frequencies of interest.

Table 4.2: Cavity Resonator Results

Material	Permittivity (ϵ_r)		Loss Tangent ($\tan\delta$)	
	Calculated	Literature	Calculated	Literature
EFI	2.77	3.6 (1 kHz)	0.166	0.03 (1 kHz)
Sylgard	2.18	2.7 (100 kHz)	0.017	0.001 (100 kHz)
Rexolite	2.33	2.53 (500 GHz)	0.004	0.002 (10 GHz)

Two 76.2 cm lines were potted containing Fair-Rite Material 43 NiZn ferrites, an EFI line and a Sylgard line. These lines were tested on the SingleLine test setup and compared with an SF_6 filled line. The lines were partially biased using a 62.2 cm bias coil located on the output end of the line. Figure 4.27 show the results for 20 kV, 30 kV, and 40 kV tests at a bias of 22.5 kA/m.

The Sylgard and EFI lines have higher peak voltages and peak to peak powers

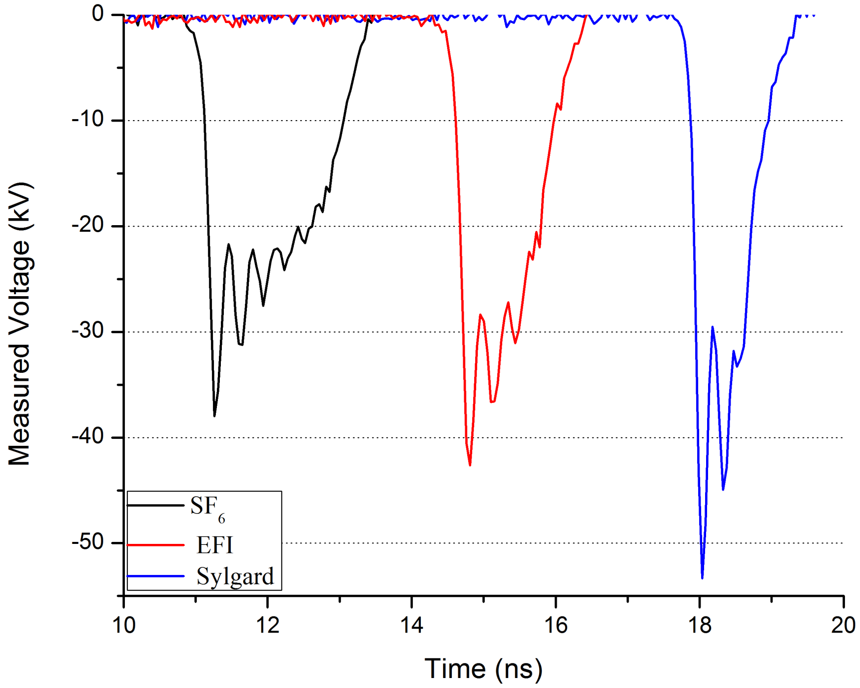

Figure 4.27: Waveforms for solid dielectric lines for a charge voltage of 40 kV.

than seen in the SF$_6$ insulated line. This is due to the fact that EFI and Sylgard have non-unity relative permittivities (Table 4.2) which causes more of the transient TEM signal to concentrate in the ferrite. This can be seen in Figure 4.28 which shows the results of a modal simulation of the each NLTL. All plots are normalized to the highest field seen which occurs in the EFI line. The magnitude of microwave oscillations in an NLTL is due to M_S, the phenomenological damping factor α, and the swing of the effective field $\vec{H}_{eff}$ from the initial state. By concentrating more of the transient field in the ferrite the swing of $\vec{H}_{eff}$ was increased. The effect of the lossy materials is evident in the increased damping of the secondary oscillations as opposed to the SF$_6$ insulated line.

Figure 4.29 shows the magnitude of the TEM magnetic field as a function of radial distance from the center of the NLTL. It can be seen that in addition to an increase in overall magnitude of the field the gradient of magnetic field along the ferrite domain

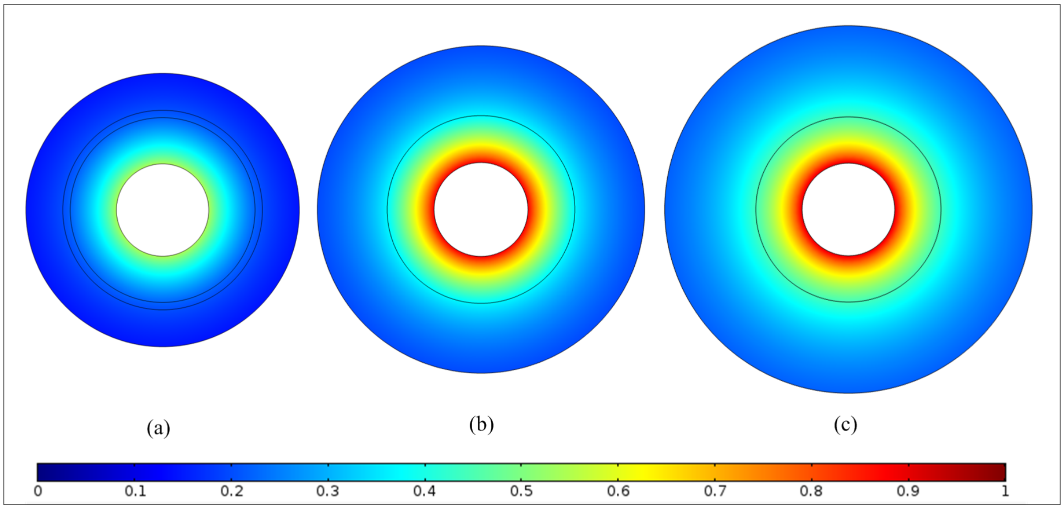

Figure 4.28: Surface plot of the magnitude of the magnetic field, normalzed to the peak magnetic field which occurs in the EFI line, inside the NLTL for (a) SF_6 line (b) Sylgard Line and (c) EFI line.

is also steepened; this should lead to an increase in the bandwidth of the generated microwave since the frequency of oscillations in given by Equation 3.1.

4.5 Coaxial High Voltage Transient Power Combiner

One method to increase total systems power is to drive two NLTLs with a common source and combine the outputs. The output voltages of the individual NLTLs can exceed 50 kV. There were no commercially available power combiners that could handle the voltage and power levels of our system. Combiners that handle the power levels needed in literature and textbooks are often resonant structures optimized for cw operation or at the very list take several cycles to load the structure [25, 26, 4]. This is not a viable option for an NLTL since the primary power exists on the first peak of the transient signal. The solution is to maintain the TEM nature of the propagating waves and combine using a coaxial transmission line structure in which two 50Ω inputs combine into a single 25Ω output line.

A schematic representation of the combiner is shown in Figure 4.30. Two NLTLs are driven by the DualGap source. Each NLTL has two biasing coils, one main bias coil 62.6 cm long and one auxiliary delay coil 14 cm long. The output of each line is

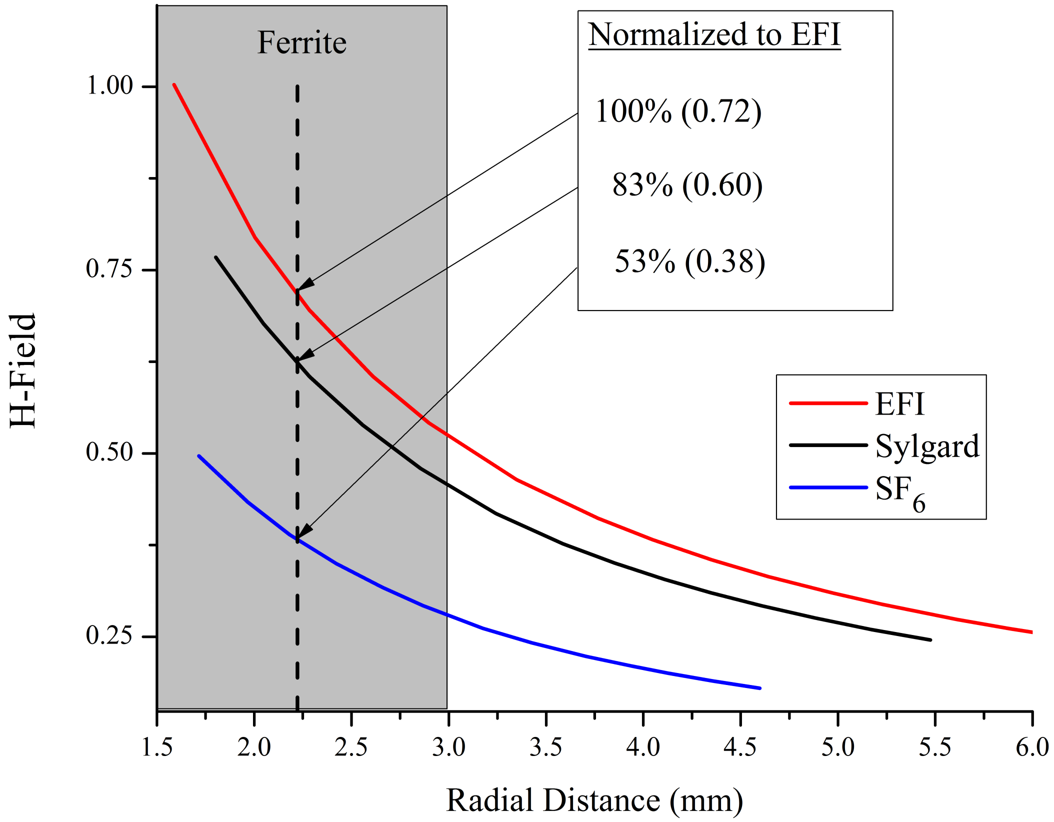

Figure 4.29: Comparison of the magnetic field seen in the coaxial line as a function of radial distance from the center of the coaxial line. The gray shaded region represents the extents of the ferrite.

connected to a 50Ω input on the combiner which connected to a single 25Ω section via a U joint, see Figure 4.31, which then tapers back to 50Ω over 14 cm by reducing the diameter of the inner conductor. The output of the combiner is connected via a delay line of LMR-600 to a 50Ω resistive load.

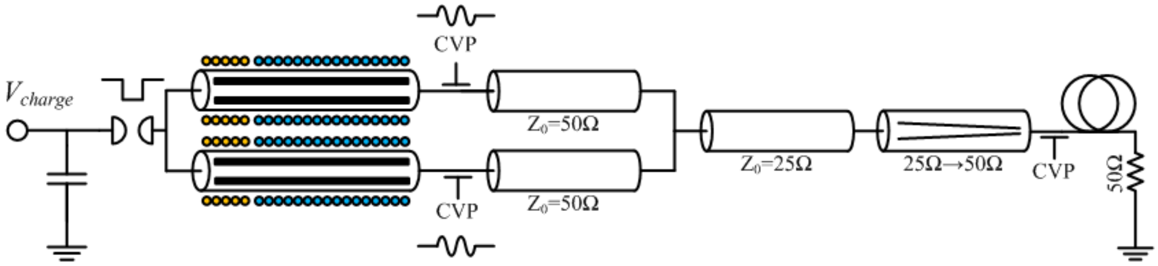

Figure 4.30: Schematic representation of coaxial power combiner. Two NLTLs drive the 50 Ω inputs of the power combiner which feeds a single 25 Ω line. The output of the power combiner tapers back to a 50 Ω impedance.

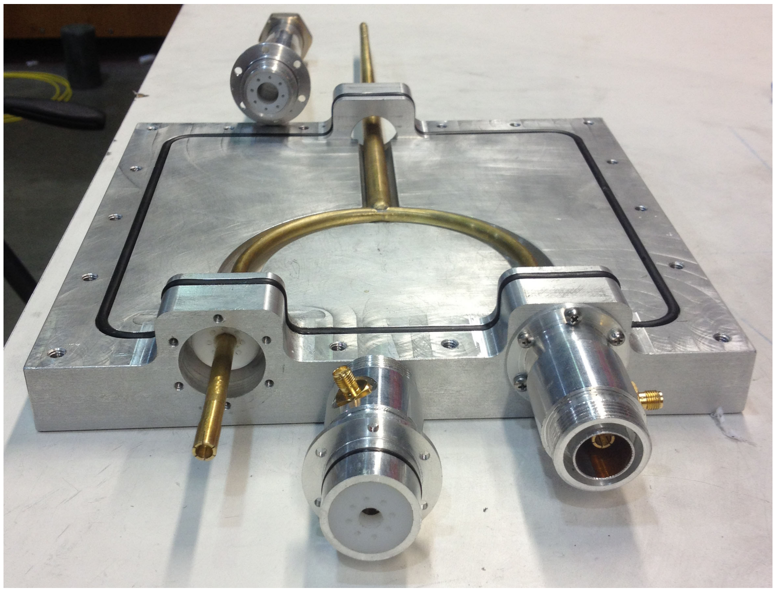

Figure 4.31: Input view of the power combiner showing the interal structure. An 8 mm hemispherical groove on the top and bottom plates form the outer conductor with a suspended section of 7 mm diamter brass forms the input conductors.

At first look it would appear the combiner would not match correctly since one input line would see a parallel combination of the other input line and output line $50\Omega \parallel 25\Omega = 16.7\Omega$. However, in the case of two matched signals, the boundary conditions at the combiner junction, the electromagnetic formulation of Kirchoff's Current Law, require that the signal pass to the output. This can be illustrated schematically in Figure 4.32 by assuming that in the case when two identical signals are incident upon the inputs, they can be considered as a single node and then can be represented as a single 25 Ω line. In practice what has been created is a combiner that passes the even-mode portion of the incident pulse and does not pass the odd-mode.

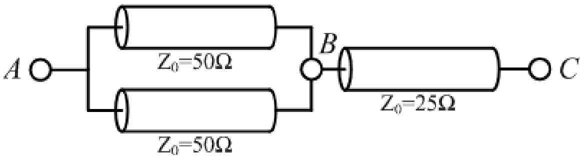

Figure 4.32: The power combiner can be represented as three transmission lines. When the signals on the input of the combiner are completely in phase the inputs can be treated as a single node, A, which will results in the input of the combiner, between A and B, looking like a single 25 Ω line.

4.5.1 Combiner Simulation

The power combiner was simulated using a transient excitation using COMSOL and the RF Module to determine the combiner effectiveness and evaluated designed features such as the impedance taper. Figure 4.33 shows the meshed power combiner structure. The results of the initial simulation show that with the input signals in phase you get all power passed to the output.

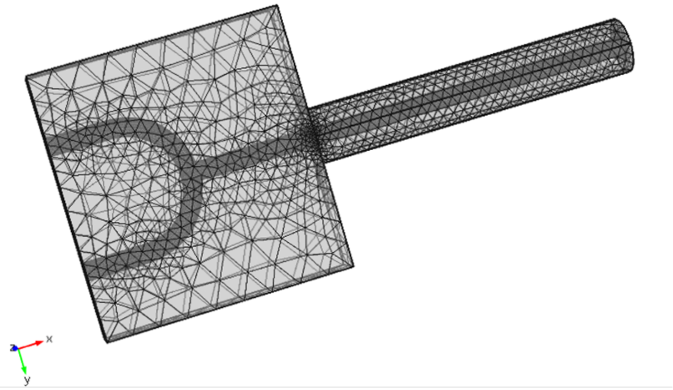

Figure 4.33: Power combiner as simulated in COMSOL. The bulk aluminum body was omitted from simulation and lumped coaxial ports used to excite the combiner.

To match the combiner output an impedance taper is required. The length of the impedance taper required will depend on the lowest wavelength of interest. Due to design constraints only tapers of less than 12 in were considered. A parametric taper geometry was programmed into COMSOL and a parametric sweep was run to determine the effect of taper length on performance. Figure 4.35a shows the taper geometry and Figure 4.35b shows the resulting S_{11} for the combiner for several taper lengths.

From Figure 4.35 it can be seen a 5.5 inch taper provides a S_{11} that is -20 dB down across the frequency range of interest. A doubling of taper length to 10 in provides only marginal improvement in S_{11} performance. The 5.5 inch taper was then simulated using the transient step excitation and the results is shown in Figure 4.36.

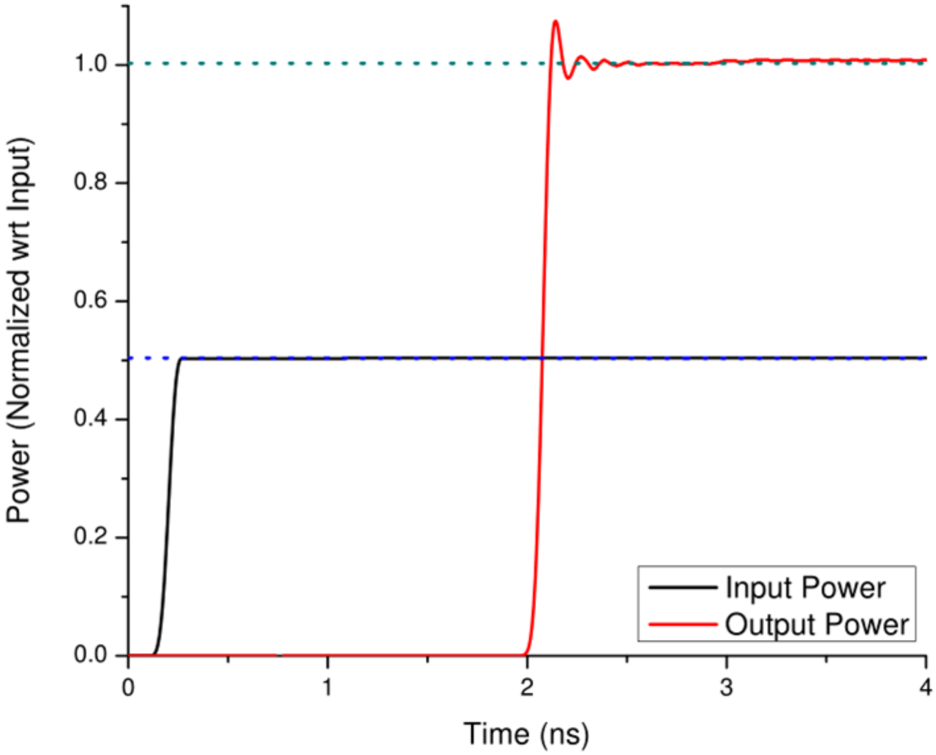

Figure 4.34: Results of ideal power combiner with no output impedance taper normalized to unity power.

4.5.2 Combiner Results

The fabricated combiner was machined out of two pieces of 2 inch and 1 inch solid Aluminum 6061 with a main body dimension of 9” x 9.5” x 2”. Pressurized SF_6 is used as an insulator with minimal dielectric support only at the input and output connectors. Silver epoxy was used on the internal surfaces to prevent RF leakage and maintain the electrical integrity of the coaxial structure.

In order to successfully combine two NLTLs, their outputs must be in phase. A simple phasing mechanism is inherent to the NLTL, nonlinear permeability. By applying a varying bias field to the NLTL the relative permeability of the ferrites is changed therefore changing the propagation velocity of the incident pulse, Equation 4.1 with c being the speed of light in free space.

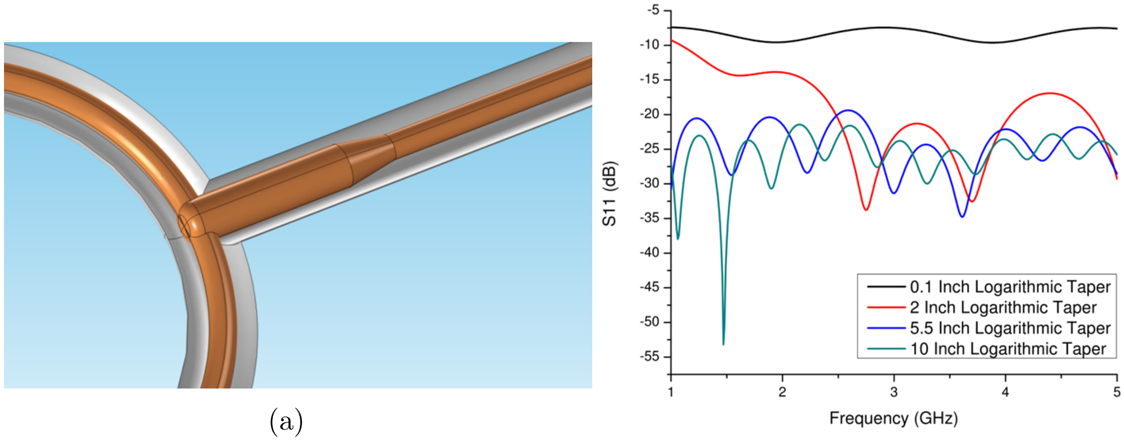

(a)

(b)

Figure 4.35: The simulation setup showing (a) parametric taper (b) the resulting S_{11} of several taper lengths.

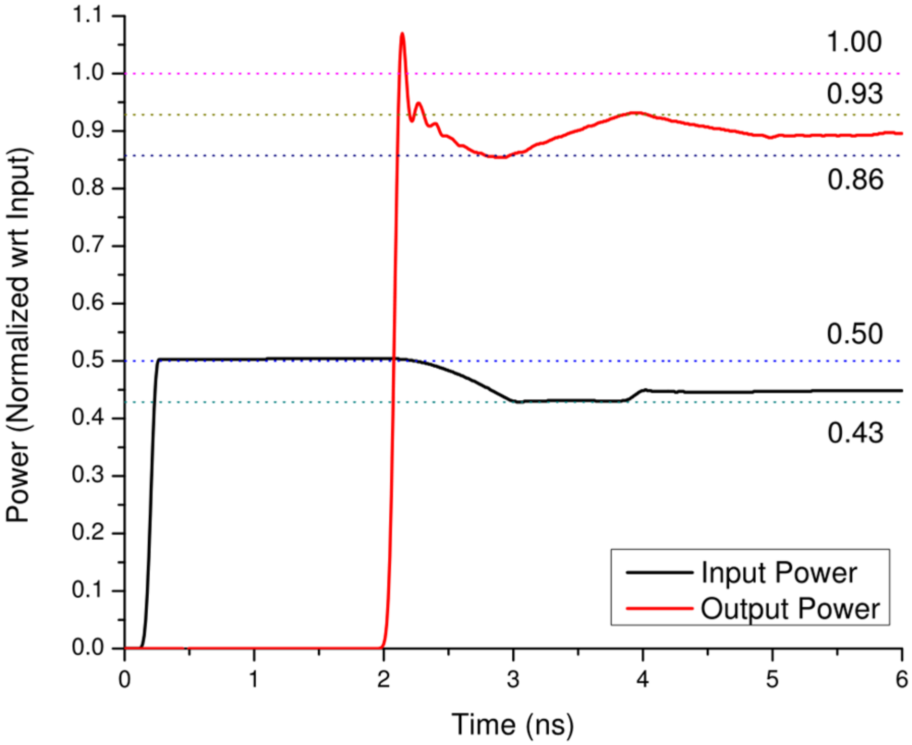

Figure 4.36: Tapered transition combiner input and output power normalized to unity. Numerical noise on the leading edge of the output power signal is ignored and the steady state response predicts combination efficiencies of 86-93 %.

$$v_p = \frac{1}{\sqrt{\mu\,\epsilon}} = \frac{c}{\sqrt{\mu_r \epsilon_r}} \tag{4.1}$$

The initial solution is to vary the bias on the existing biasing coil of each NLTL until they are in phase. This was effective in creating a delay between the NLTLs, however, since the microwave frequency and magnitude are dependent on the effect magnetic field, this method resulted in two pulses of different magnitudes and center frequencies arriving at the combiner. To fix this problem a two coil solution is used where one large main biasing coil and a second smaller delay coil is placed on the input of the NLTL. By altering the bias field in this smaller delay coil varying delays could be achieved without drastically altering the output waveforms, although small differences will be present. Schematically this can be seen in Figure 4.30 and pictured in Figure 4.39.

A delay test was conducted to determine if the small coil that was designed could delay the signal enough to bring two out of phases NLTLs into alignment. The test was conducted with the SingleLine gap test setup and MX7 ferrites. The oscilloscope was triggered off the falling edge of the spark gap output waveform at a fixed level and shots were taken at several bias fields on the delay coil. The peak locations of the output waveforms were compared to determine the delays achieved. Figure 4.37 shows an example plot of the output waveforms and Figure 4.38 shows the delay as a function of applied field for 20 kV, 30 kV, and 40 kV charge.

At charge voltages of 20 kV to 30 kV a bias field of 5 kA/m or higher can shift a waveform by over 300 ps. This is half the period of a 1.5 GHz signal, the lower frequency typically observed in our lines. The 40 kV charge voltages only required a few kA/m to create delays of 400 ps and higher. The coils are able to effectively delay the lines long enough to bring two out of phase NLTLs into alignment.

The combiner testing was carried out using the recently acquired YIG ferrites since they were the most numerous of the Metamagnetics ferrites available and showed the longest period of oscillations, allowing a better test of the even-mode and odd-mode

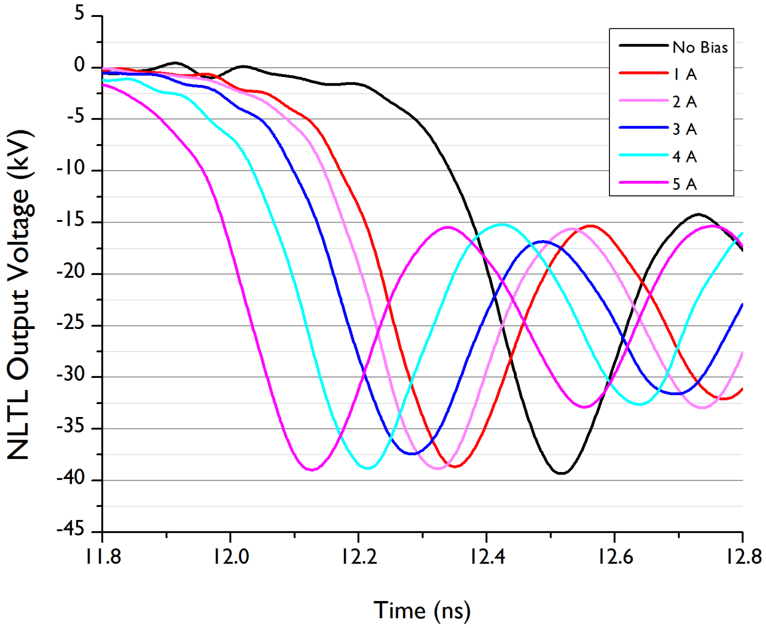

Figure 4.37: Average delays for several shots of the NLTL as measured from spark gap pulse to peak of the output waveform. Data shown is for a 62.2 cm main coil and 14 cm delay coil.

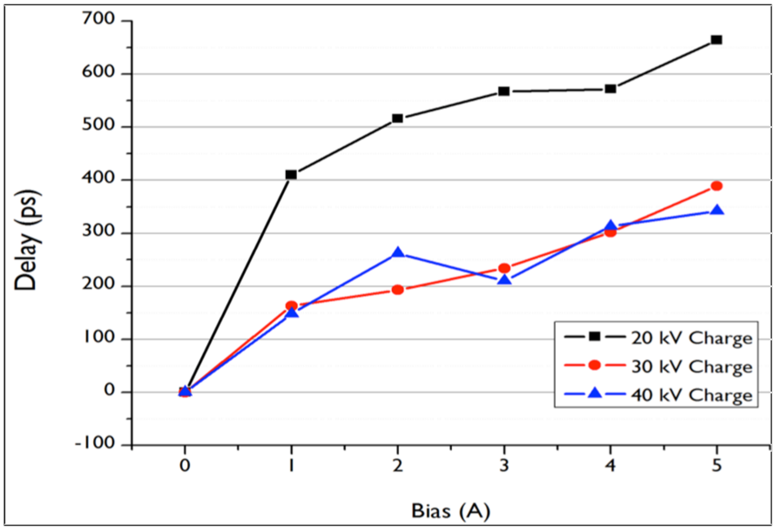

Figure 4.38: Delay as a function of applied field for several charge voltages using a 62.2 cm main coil and 14 cm delay coil..

discrimination properties of the combiner. Three charge voltages were tested 20 kV, 30 kV, and 40 kV with biases of 15 kA/m and 20 kA/m. The output of the combiner was measured on the LMR-600 delay line using probe LMR4 and the inputs were monitored on the built in combiner probes CMB1 and CMB2. The test setup is pictured in Figure 4.39. The in-phase results are shown in Figures 4.40-4.42.

Figure 4.39: Combiner test setup.

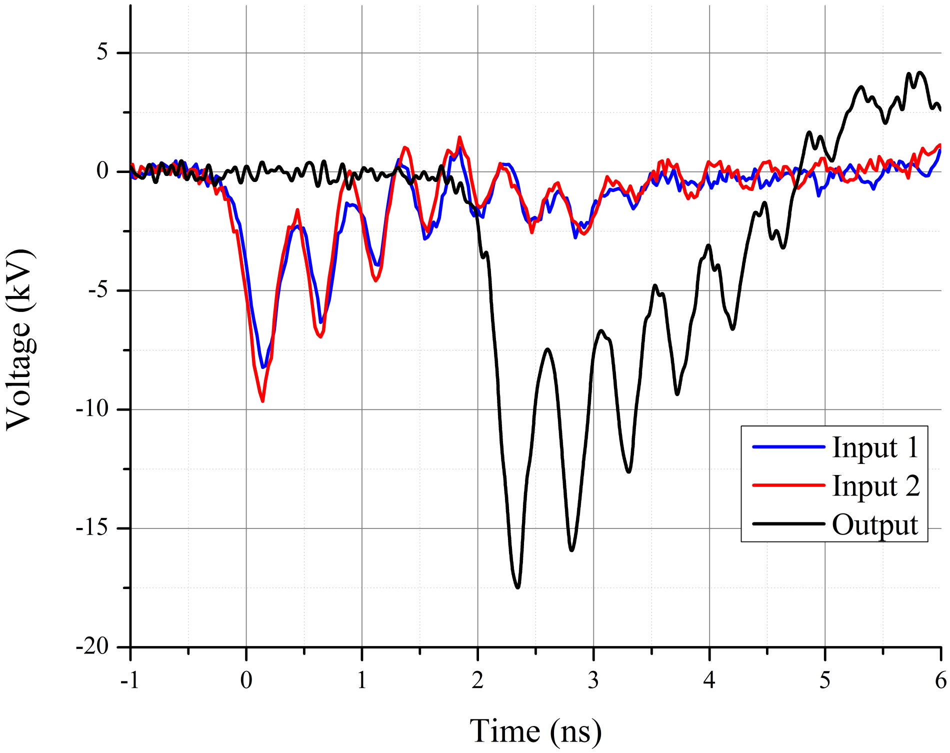

Figure 4.40: 20 kV combiner results showing the the input signals in blue and red and the output in black. The signals are shifted in postprocessing.

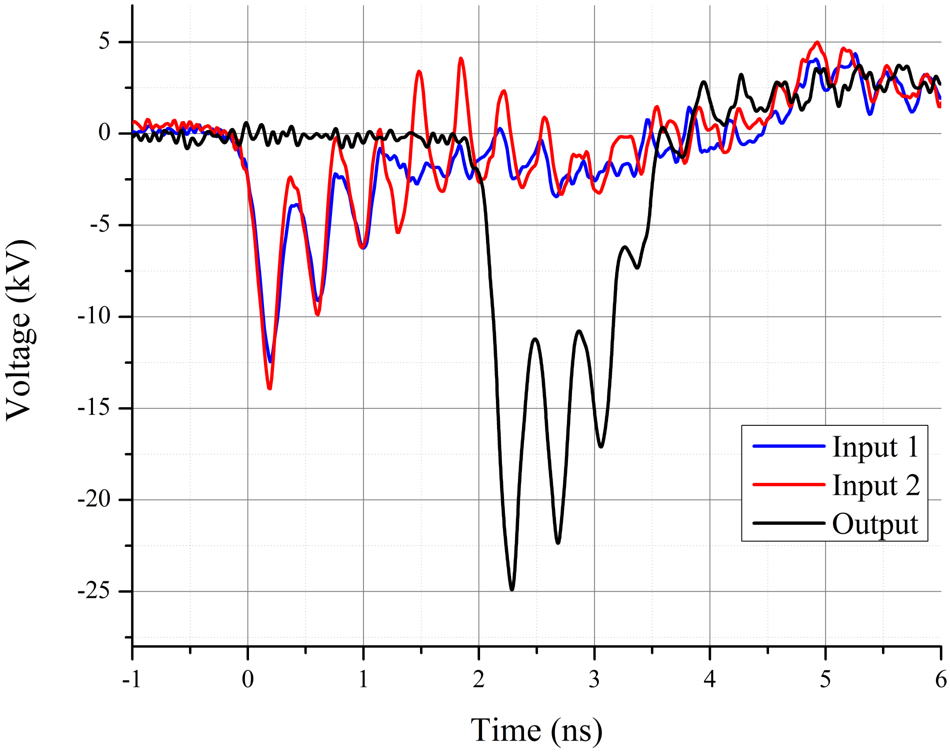

Figure 4.41: 30 kV combiner results showing the the input signals in blue and red and the output in black. The signals are shifted in postprocessing.

The combination was best at 20 kV and 30 kV which is to be expected as that is the range at which the YIG ferrites operate the best and are most repeatable. The peak power combination number is calculated by squaring the measured peak voltage ratio calculated using Equation 4.2. The voltages probes are both located on sections of 50 Ω coaxial cable therefore the voltage to current ratios are consistent and the power calculation is valid.

$$V_{peak} = \frac{V_{out}^{peak}}{V_{in1}^{peak} + V_{in2}^{peak}} \tag{4.2}$$

The simulation results given in Table 4.3 agree with the predicted simulation range of 86-93 % from the COMSOL simulation. Future verification of combiner performance will be conducted using an rf amplifier and dual output network analyzer to probe a wider range of frequencies and corroborate the NLTL results.

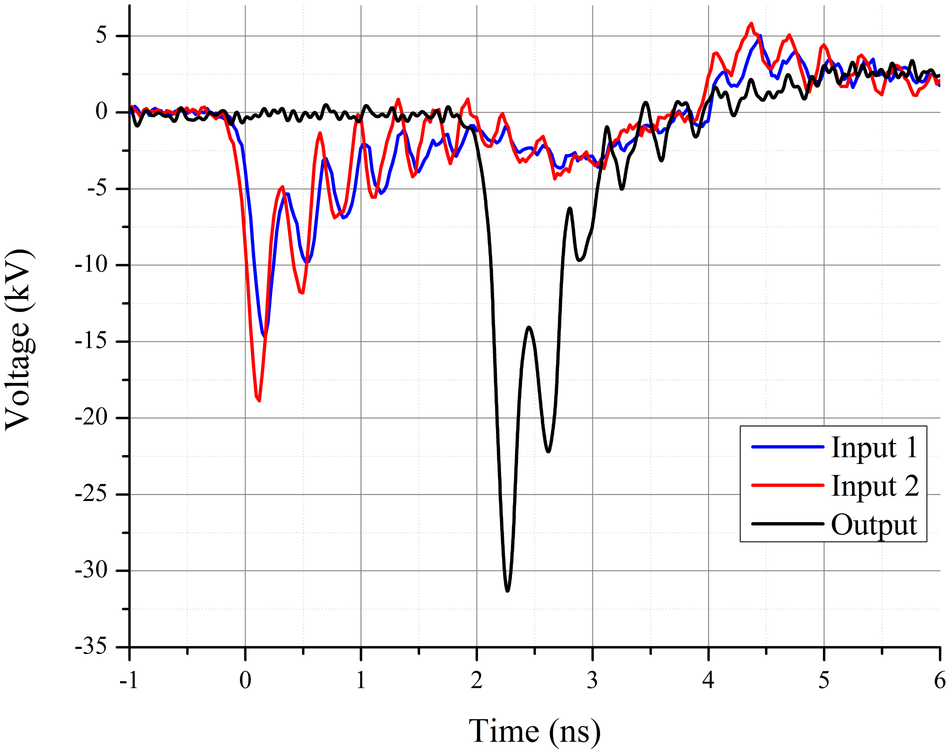

Figure 4.42: 40 kV combiner results showing the the input signals in blue and red and the output in black. The signals are shifted in postprocessing.

Table 4.3: Combiner Results

Charge Voltage (kV)	Main Bias (kA/m)	Delay Bias (kA/m)	Peak Voltage (%)	Peak Power (%)
20	17.70 (A)	22.22 (A)	97.9	95.8
30	17.70 (A)	24.08 (A)	94.4	89.1
40	12.91 (A)	31.26 (A)	93.3	87.0

CHAPTER 5

ARRAY TESTING

In order to deliver the microwave power generated by an NLTL to a remote target an antenna is required. The signal is a transient pulse of durations between 1-10 ns with most of the microwave power contained in the first few cycles, therefore a resonant structure would not be an efficient radiator. A TEM Horn is a traveling wave structure and as such is well suited to the application.

5.1 Individual Element

The NLTL is a shielded coaxial structure. In order to radiate the signal carried inside, the coaxial line must be converted into a structure that exposes the signal while incurring minimum reflections. Additionally, the radiating element must have balanced currents on both surfaces in order to radiate efficiently. This transition is accomplished by the use of a balun. Most baluns are designed for cw sources and take advantage of resonant effects, which will not work for a transient signal of a few cycles.

Another option is to employ a balun based on the theory of small reflections. A zipper balun opens up from a fully enclosed line to a parallel plate configuration gradually and thus the characteristic impedance changes slowly. Each point on the balun sees only a small difference in Z_0 and therefore has s small reflection. If the taper is taken to be long enough a balanced parallel plate output can be achieved. The parallel plate output is a perfect feed-in for a TEM horn antenna. The zipper balun is described in [27] which provides a closed form solution for balun impedance up to 120 degrees, after that a COMSOL simulation determined the characteristic impedance. A parallel plate section was designed according to Equation 5.1, where η is the effective characteristic impedance of the medium, and h is the height and w is the width of the parallel plate respectively, which transitions into a TEM horn. The TEM horn aperture was specified to by 5" x 5" and a taper to the output impedance over a distance of 7 inches was created. Figure 5.1 shows the resulting antenna. Connections are made using a standard 7/16 connector which allows the antenna to be hooked up to diagnostics using standard adaptors. A gas port on the antenna feed allows for SF_6 backfill for hv operation.

$$Z_0 = \sqrt{\frac{\mu}{\epsilon}}\frac{h}{w} = \eta\frac{h}{w} \tag{5.1}$$

The inner conductor is surround by an Rexolite 1422 insulator. The design formulas from [27] assume a homogenous dielectric both inside and outside of the coaxial structure. To maintain a similar dielectric constant the antenna was potted in Sylgard 184 which has a relative permittivity of 2.7 which is close to that of Rexolite at 2.53. The Sylgard also provides the required hold off in the feed of the antenna until the horn opens up enough to allow air to hold off the pulsed voltages. A CAD drawing is shown in Figure 5.1 and the two fabricated antennas are pictured in Figure 5.2.

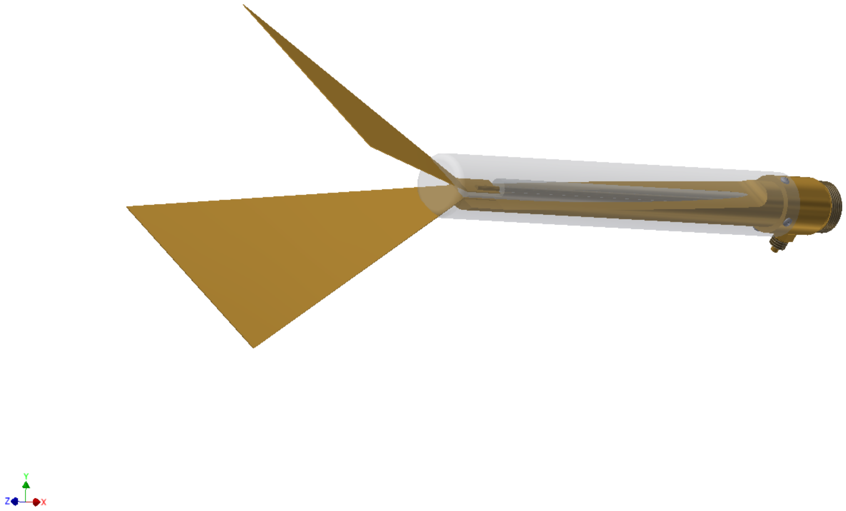

Figure 5.1: 3D CAD Model of the 5 inch TEM horn antenna with zipper balun.

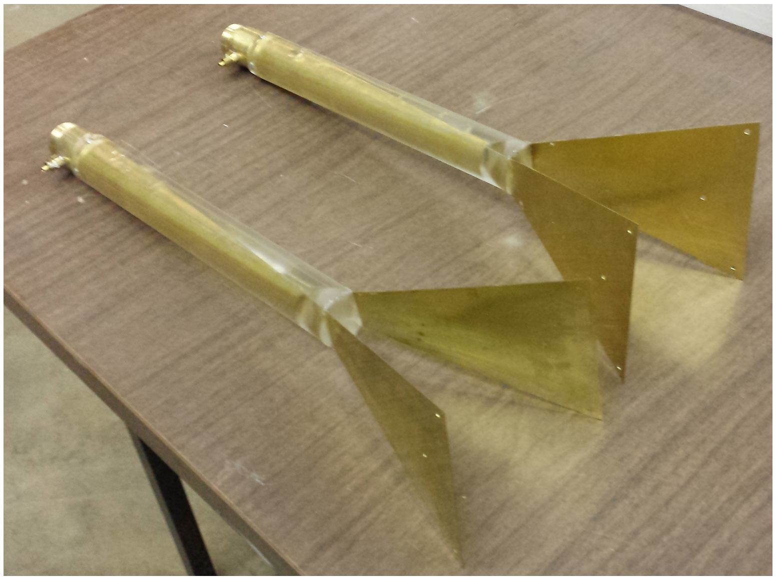

Figure 5.2: Two fabricated TEM horn antennas used for array testing.

5.1.1 Element Testing

The S_{11} of each antenna was measured using a network analyzer from 500 MHz to 6 GHz, results are shown in Figure 5.4. A COMSOL simulation was run to determine the radiation pattern of the element to compare to experimental results. The individual element model and two-element array model are shown in Figures 5.3a and 5.3b respectively.

An A. H. System SAS-571 Double Ridge Horn was used as a receiving antenna. A comparison of the radiated signals of each TEM horn is shown in Figure 5.5. Data was collected at 2 m at angles of 0^o, 10^o, 15^o, 20^o, 25^o, and 30^o. The COMSOL simulation result of the TEM horn at 2.3 GHz is plotted against the collected data points in Figure 5.6. The experimental results are less directive than the simulated horn and this discrepancy may be due to leakage from the balun.

5.2 Array Results

The DualGap was used to drive two TEM horns connected to the NLTL outputs using a length of LMR-600 delay line. A wideband TEM horn located 2 m away was used as a receiving antenna. The receiving horn has a known gain and along with

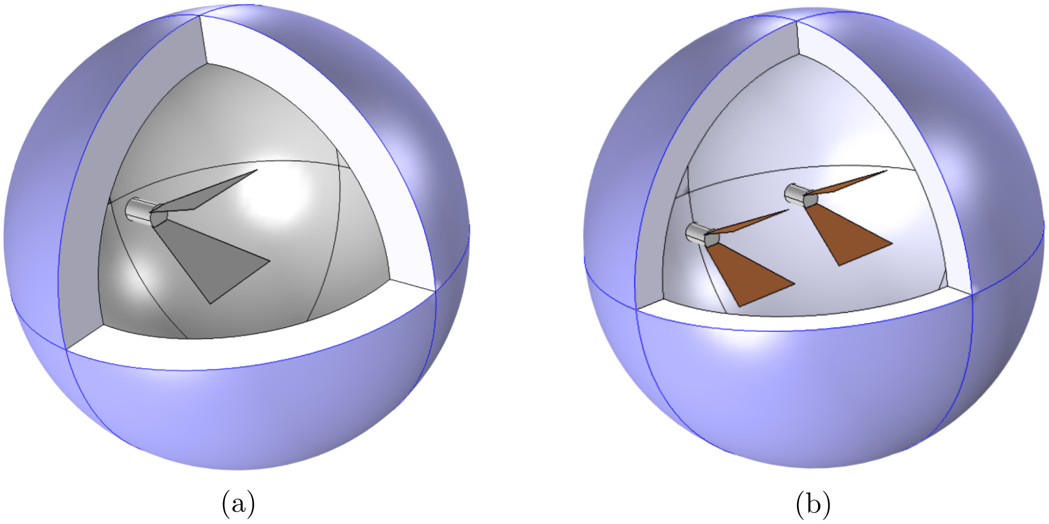

Figure 5.3: Models used to simulate (a) single TEM horn and (b) a two element TEM horn array.

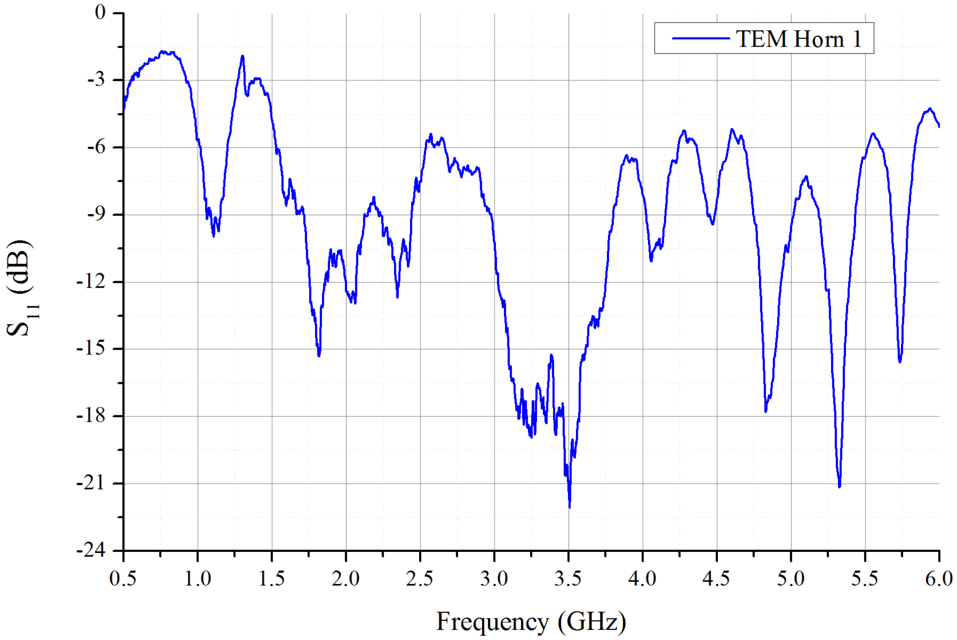

Figure 5.4: S_{11} of a single TEM Horn swept from 500 MHz to 6 GHz. There are regions of sub 10 dB reflection centered at 2 GHz and 3.25 GHz.

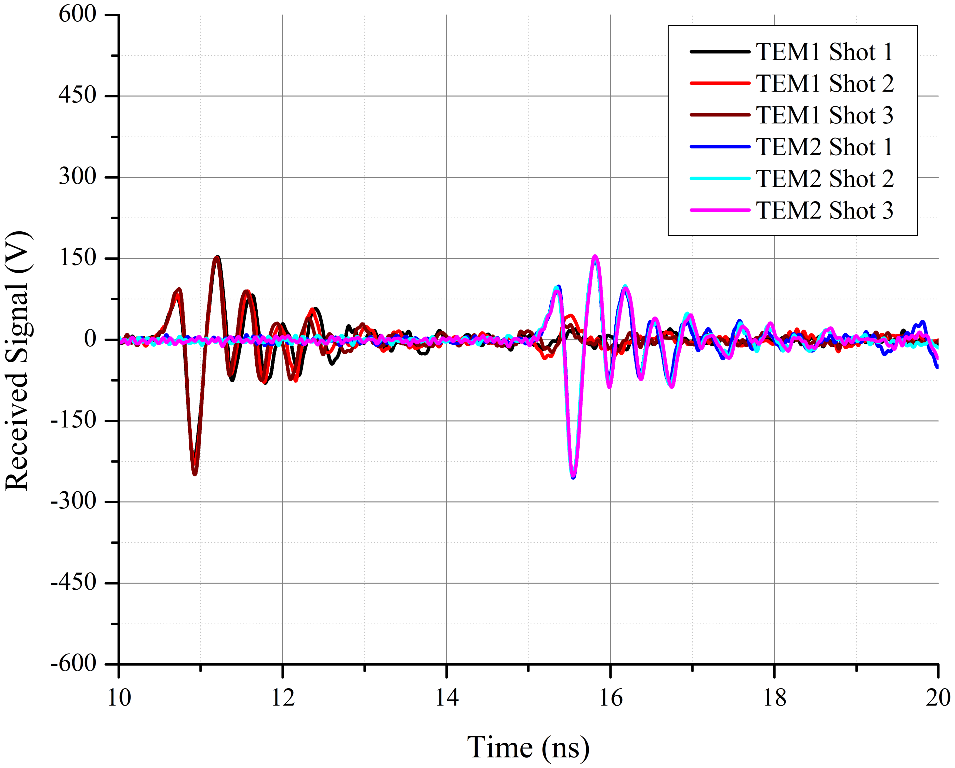

Figure 5.5: Received raw signal from TEM Horn 1 and TEM Horn 2

the S_{11} data the individual elements can be calibrated. With the individual elements calibrated, the array performance can be evaluated using the closed form solution of the array factor from Chapter 2 and the element pattern from Section 5.1.

First, the receiving antenna is placed at the centerline of the array and both elements are excited in phase to determine the baseline for the Array pattern. Three separate beam steering angles are tested, 0°, 10°, and 20°. In each case the bias is adjusted until a maximum received signal is obtained. One a maximum is obtained the bias is held constant and pattern sweep is conducted at teh same angles as the individual element testing. Figure 5.9 shows the peak received waveforms for each angle. The time-resolved electric field strength is plotted in Figure 5.7. The array field is more than twice as large as the single element field. This is most likely due to the fact that in order to align the NLTL pulses the bias on line 2 had to be increased, this means a higher bias field which may lead to more of the incident spark gap pulse

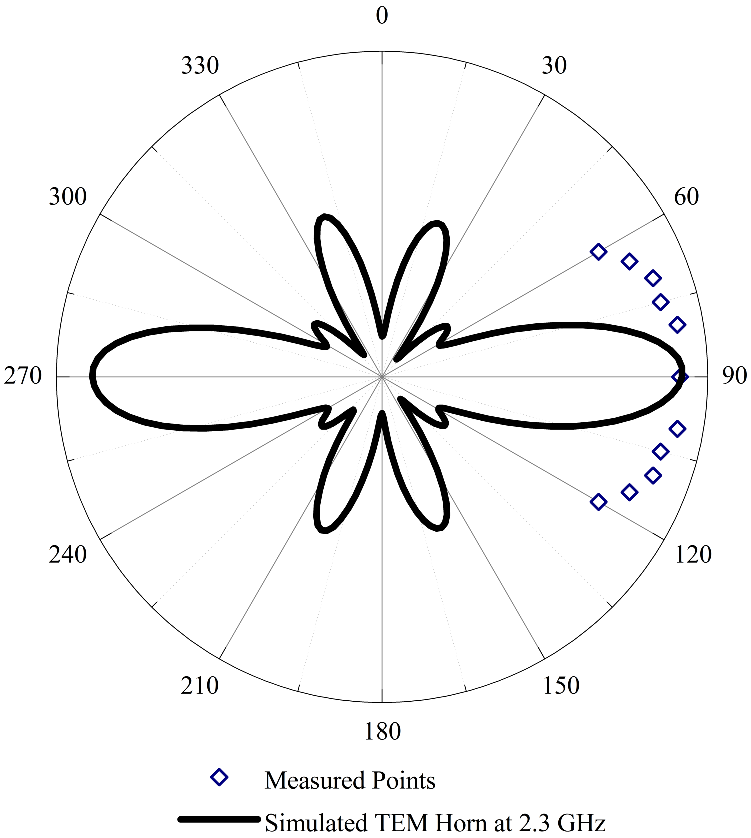

Figure 5.6: Simulated element pattern at 2.3 GHz compared to experimental results. Both patterns are normalized.

getting into the line thus resulting in a larger voltage than what appears on the single TEM horn.

The results of the two element array are shown in Figure 5.8. The main beam is reconstructed very well however there is variation from simulation in the main side lobes. This difference is most likely caused by the discrepancy in the element pattern described above.

5.2.1 Four Element Array

Future testing of the array will use the MultiLine gap to drive four elements at once. A system drawing is shown in Figure 5.10. Each antenna will be connected using an LMR-600 delay cable allowing for variation of inter-element spacing depending on operating frequency.

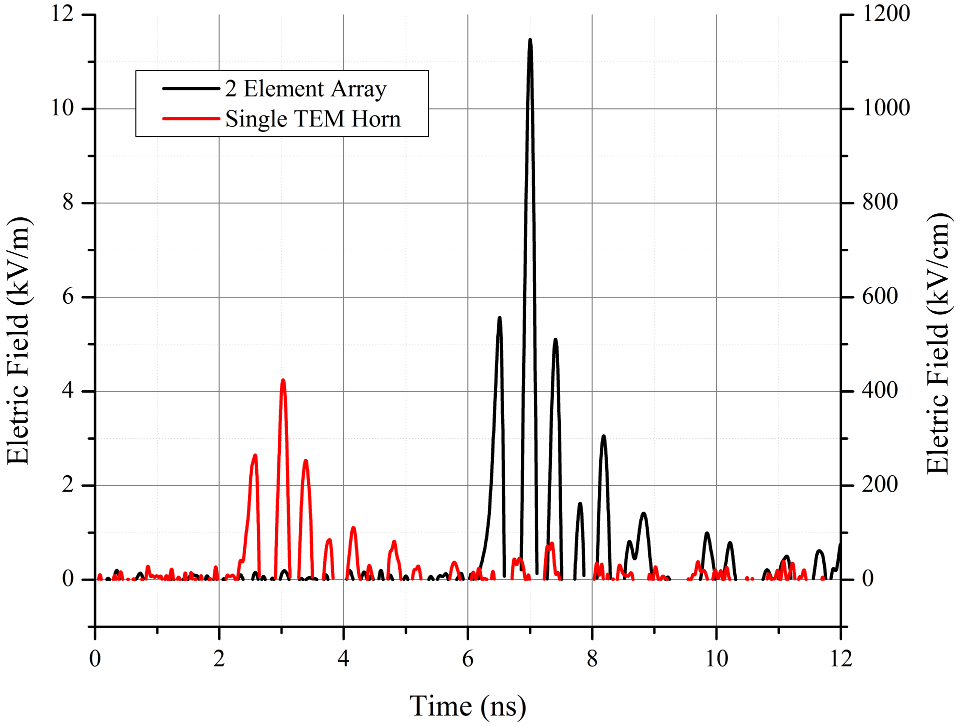

Figure 5.7: Measured electric field strength for a single TEM Horn and a two element array.

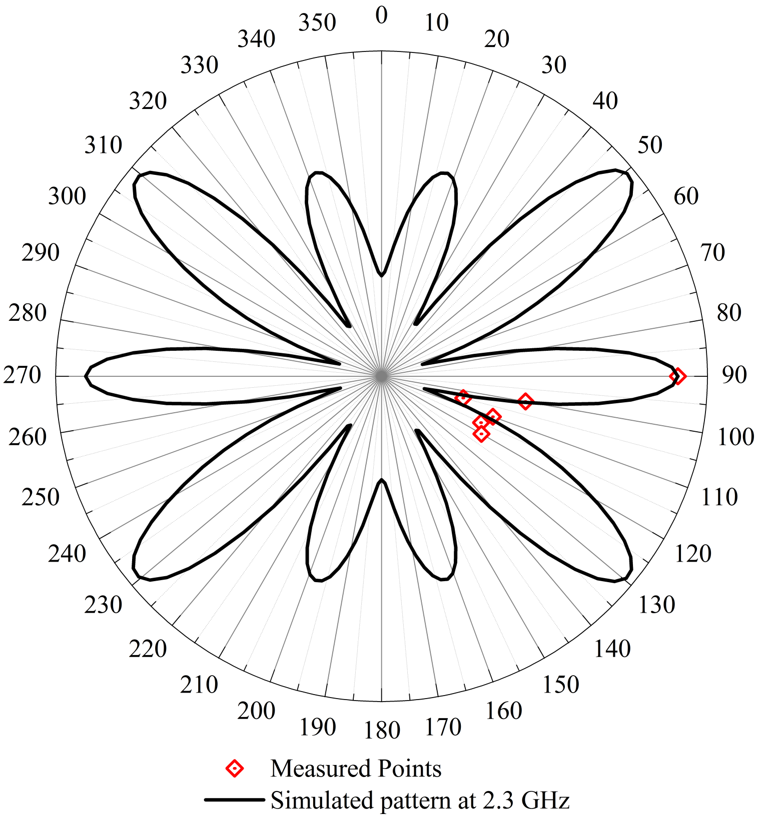

Figure 5.8: Simulated array pattern for an inter-element spacing of 23 cm at 2.3 GHz compared to experimental results. Both patterns are normalized to the peak value occuring a the 90°point of the H-Plane pattern.

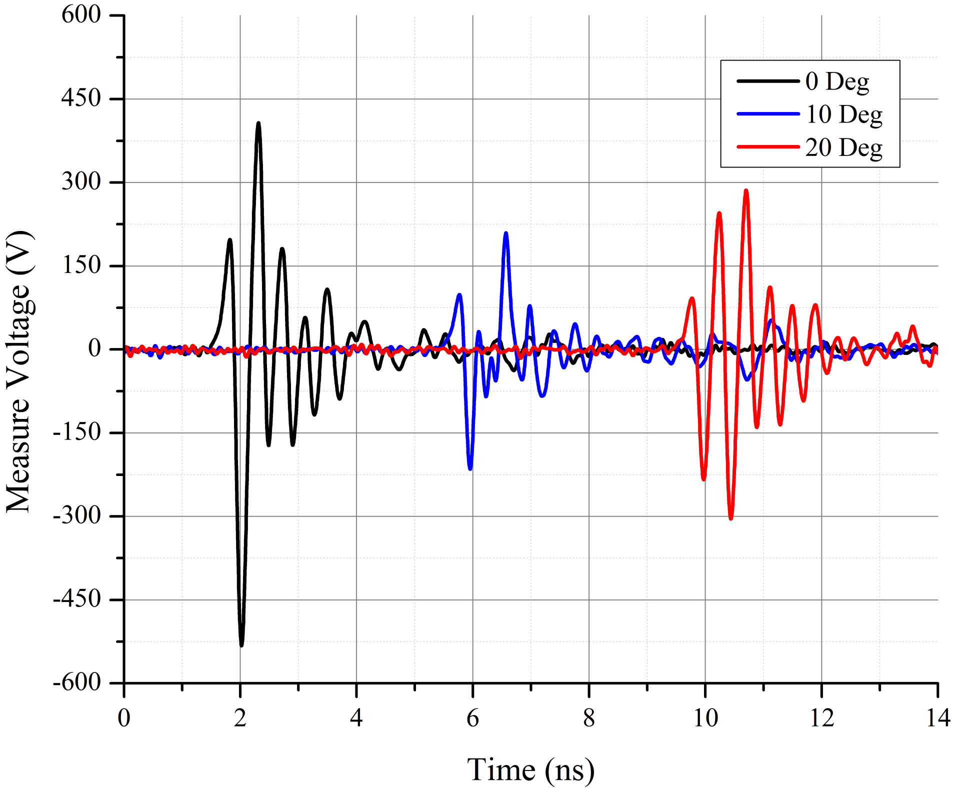

Figure 5.9: Raw voltage of peak received waveforms collected at 2 m from array centerline.

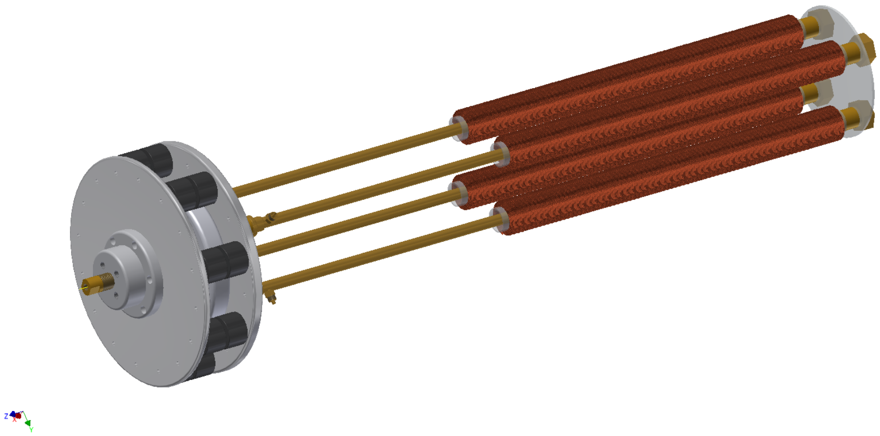

Figure 5.10: System of four NLTLs being driven via the MultiLine gap. Each NLTL output is connected to a TEM horn via a delay line.

CHAPTER 6

FINITE ELEMENT METHOD SIMULATION OF NONLINEAR TRANSMISSION LINES

Due to the complex interdependence of geometry, bias fields, and the incident pulsed fields on NLTL performance it is difficult to predict performance via analytical means. An NLTL simulation is therefore desirable in order to predict performance due to changes in the experimental setup. A Finite Element Method (FEM) simulation was developed using COMSOL$^{\text{TM}}$.

6.1 Simulation Setup

As discussed in Chapter 3 the precession of magnetic moments in the ferrimagnetic material is the source of the microwave oscillations. In Section 2.1.1 two equations of motion were introduced to describe the precessional motion: the Landau-Lifshitz and the Landau-Lifshitz Gilbert. Both equations are qualitatively similar, however when the LLG equation is transformed into the LL form, given in Equation 6.1, a difference is apparent for large values of the damping factor α [6, 1].

$$\frac{d\vec{M}}{dt} = \frac{\gamma}{1+\alpha^2}\left[\vec{M}\times\vec{H}\right] + \frac{\alpha\gamma}{(1+\alpha^2)\,M_s}\left[\vec{M}\times\left(\vec{M}\times\vec{H}\right)\right] \tag{6.1}$$

When in the LL form the LLG no longer contain a time derivative on the Right Hand Side (R.H.S.) of the equation. This double cross-product form which is the same as seen in the LL equation allows for a direct comparison of the equations behavior. Equations 6.2 and 6.3 show the difference in the Coefficient of Precession C_P, proportional to $\vec{M}\times\vec{H}$, and the Coefficient of Damping C_D, proportional to $\vec{M}\times\left(\vec{M}\times\vec{H}\right)$, between the two equations.

$$C_P^{LLG} = \frac{\gamma}{1+\alpha^2} \qquad C_D^{LLG} = \frac{\alpha\gamma}{(1+\alpha^2)\,M_s} \tag{6.2}$$

$$C_P^{LL} = \gamma \qquad C_D^{LL} = \frac{\alpha}{M_s} \tag{6.3}$$

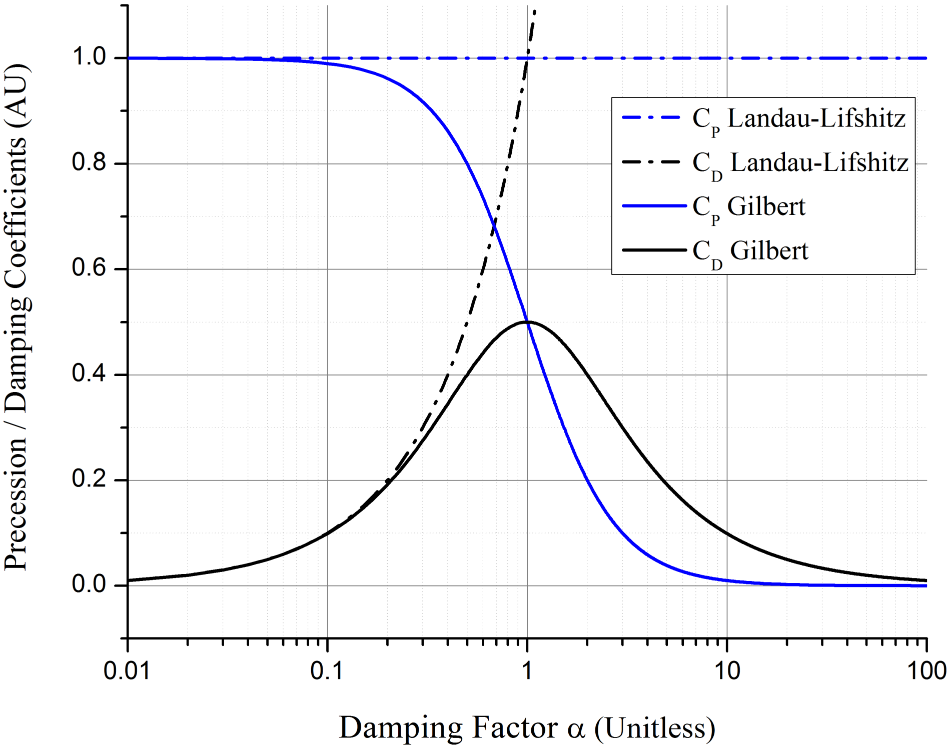

Figure 6.1: Behavior of the Precession Coefficient C_P and the Damping Coefficient C_D as the unitless damping factor α increases. Reproduced from [6]

In order to simulate the LLG equation in COMSOL the equation must be broken down into vector components. The simulation geometry is in cylindrical coordinates so carrying out the cross products and collecting terms gives Equations 6.4 - 6.6 where C_P and C_D are given in Equation 6.2 with the superscript omitted.

$$\frac{dM_r}{dt} = C_P\left(H_\phi M_z - H_z M_\phi\right) + C_D\left[M_\phi\left(H_r M_\phi - H_\phi M_r\right) - M_z\left(H_z M_r - H_r M_z\right)\right] \tag{6.4}$$

$$\frac{dM_\phi}{dt} = C_P \left(H_z M_r - H_r M_z\right) + C_D \left[M_z \left(H_\phi M_z - H_z M_\phi\right) - M_r \left(H_r M_\phi - H_\phi M_r\right)\right] \tag{6.5}$$

$$\frac{dM_z}{dt} = C_P \left(H_r M_\phi - H_\phi M_r\right) + C_D \left[M_r \left(H_z M_r - H_r M_z\right) - M_\phi \left(H_\phi M_z - H_z M_\phi\right)\right] \tag{6.6}$$

The moments precess around an effective magnetic field, H_{eff}, which is given by Equation 6.7. The first term represents the exchange field discussed in Chapter 2 and the second term represents the anisotropy field. The first two terms are neglected since the simulation assumes an isotropic ferrimagnetic material and the exchange constant A is too short of a range to be considered on a macroscopic scale. This assumption is valid if the conditions discussed in Section 2.1.2 are satisfied.

$$\vec{H}_{EFF} = \frac{2\mu_0}{m_s}\nabla \cdot (A\nabla m) + \frac{1}{\mu_0 M_s}\frac{\partial E_A}{\partial m} + \vec{H}_D + \vec{H}_{EXT} \tag{6.7}$$

What remains is an effective field that is a superposition of the applied bias field and transient pulse, given by H_{EXT} and the demagnetizing field created by the magnetic domains, given by H_D, given in Equation 6.8.

$$\vec{H}_{EFF} = \vec{H}_D + \vec{H}_{EXT} \tag{6.8}$$

6.2 COMSOL Model Setup

The COMSOL software package comes with several different simulation modules which in turn contain separate physics instances. In the NLTL simulation three module are used: the RF module, the AC/DC module, and the Mathematics module. The setup of each module is discussed below.

The symmetry of a coaxial NLTL is utilized by simulating a 2D axi-symmetic model which significantly reduces the degrees of freedom of the simulation. The axi-symmetric model is setup using cylindrical coordinates and assumes no spatial variation in the azimuthal direction, that is $\frac{\partial \mathbf{W}}{\partial \phi} = 0$ where $\mathbf{W}$ is a simulation parameter being solved for. Figure 6.2 shows the NLTL geometry to be simulated; by taking a slice of the structure you get the axi-symmetric geometry shown in Figure 6.3.

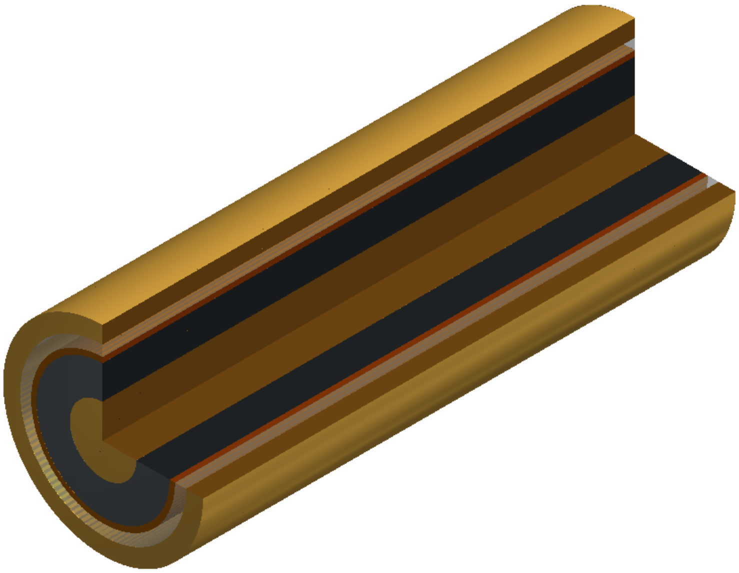

Figure 6.2: Three-quarter view of an SF_6 line. A slice along the plane of the 3D structure give the 2D axi-symmetric geometry of Figure 6.3

A few changes from the physical NLTL were made to simplify simulation. First the 10 mil thick polyimide sleeve was removed. The smallest feature of a model can dictate the mesh density for the entire geometry and therefore the inclusion of such a small feature increases the degrees of freedom of simulation without changing the physical solution. Second, a dummy insulating region, referred to as 'insulator' in Figure 6.3 is introduced at either end of the structure. This is physically similar to the teflon spacers present in the NLTL but more importantly serves to move the Lumped Port feature away from the end of the ferrite. A Lumped Port is expecting a coaxial mode and thus would disturb the fields at the boundary between the ferrite and insulating material.

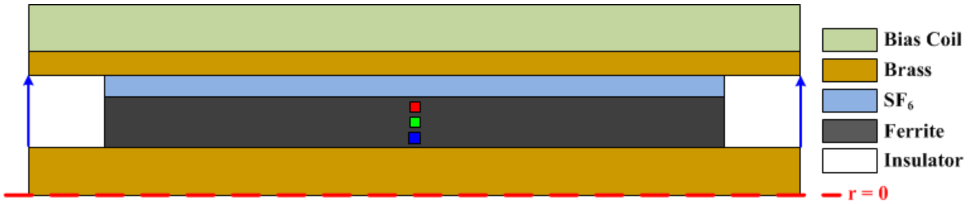

Figure 6.3: Cross-section of the simulation geometry. The polyimide film is omitted and dummy dielectric is inserted at either end of the NLTL. Axially symmetry is delineated by the dashed red line and Lumped Ports by blue arrows. The inner, middle, and outer points referred to in Figure 6.5 are shown as points in blue, green, and red respectively.

6.2.1 Mathematics Module - LLG Equation

The LLG equation, as given in the form of Equations 6.4 - 6.6, is solved using the Time-Dependent Domain ODEs (dode) and DAEs physics interface of the Mathematics Module in COMSOL. The dode solves Equation 6.9 only in the specified domains, where $\mathbf{u}$ is the vector quantity being solved for, $\mathsf{e_a}$ and $\mathsf{d_a}$ are the coefficient tensors, and f is the forcing tensor. Using Equations 6.4 - 6.6 we can fill in the coefficient tensors according to Equations 6.9 and 6.10 and assigning the R.H.S. to f.

$$e_a \frac{\partial^2 \mathbf{u}}{\partial t^2} + d_a \frac{\partial \mathbf{u}}{\partial t} = f \tag{6.9}$$

$$\mathbf{u} = \begin{pmatrix} M1 \\ M2 \\ M3 \end{pmatrix} \qquad e_a = \begin{pmatrix} 0 & 0 & 0 \\ 0 & 0 & 0 \\ 0 & 0 & 0 \end{pmatrix} \qquad d_a = \begin{pmatrix} 1 & 0 & 0 \\ 0 & 1 & 0 \\ 0 & 0 & 1 \end{pmatrix} \tag{6.10}$$

This simple method of entry is a benefit of converting the LLG equation into the LL form and therefore removing the time derivative on the R.H.S. of the equation. This equation is solved only for the Ferrite domain where $M1 = M_r$, $M2 = M_\phi$, and $M3 = M_z$ represent the magnetic moments of the material.

The initial condition of the domains in the ferrites are either set to be all initially aligned with the bias field, i.e. $M1 = 0$, $M2 = 0$, and $M3 = M_S$, or uniformly aligned without a preferred direction $M1 = .5774M_S$, $M2 = .5774M_S$, and $M3 = .5774M_S$. The factor of 0.5774 ensures that the magnitude of $\vec{M}$ remains constant and equal to

M_S.

The motion of the magnetic moments is determined by the effective field $\vec{H}_{eff}$, named $Hephi$, Her, and Hez in the simulation. This field is specified as a variable in COMSOL in order to take into account both the magnetic field of the bias field (Section 6.2.2) and the transient voltage pulse (Section 6.2.3). COMSOL uses the convention of naming internal variables as a the module prefix, e.g. temw, dode, or mf, followed by the name of the variable, that convention is used here to explicitly define the coupling of the models, Equations 6.11-6.13.

$$Hephi = temw.Hr + mf.Hr \tag{6.11}$$

$$Hephi = temw.Hphi + mf.Hphi \tag{6.12}$$

$$Hephi = temw.Hz + mf.Hz \tag{6.13}$$

Two constraints are specified: A point-wise constraint is imposed to ensure that the value of the magnetization does not change during the simulation, Equation 6.14, and Brown's condition, Equation 6.15, that requires the spatial variation of the magnetization normal to the boundary to be zero.

$$M_S - \sqrt{M_r^2 + M_\phi^2 + M_z^2} = 0 \tag{6.14}$$

$$\frac{\partial \vec{M}}{\partial \vec{n}} = 0 \tag{6.15}$$

6.2.2 AC/DC Module - Bias Field

In order to create the static bias field the AC/DC module is used. The Magnetic Fields (mf) physics interface provides a Single Turn Coil Domain where a current density can be specified to simulate a solenoidal field within the NLTL. The mf interface is solved on all domains at the outset of the simulation using a Stationary step in the solver. This data can be saved for use in the rest of the model since the bias field is a constant.

6.2.3 RF Module - Transient Propagation

In order to see a voltage on the output of the NLTL the moments must excite transient modes that propagate down the line. The RF Module with the Time-Dependent Transient Electromagnetic (temw) physics interface is used for this purpose. The temw module solves for the magnetic vector potential according to Equation 6.16.

$$\nabla \times \frac{(\nabla \times \mathbf{A})}{\mu_r} + \mu_0 \sigma \frac{\partial \mathbf{A}}{\partial t} + \mu_0 \frac{\partial}{\partial t}\left(\epsilon_r \epsilon_0 \frac{\partial \mathbf{A}}{\partial t}\right) = 0 \tag{6.16}$$

In addition to Equation 6.16 COMSOL allows the user to specify the constituent relations to be used in each domain. This allows us to couple in the motion of the magnetic moments solved for by the LLG solver. In all domains the constituent relationship of the electric field is $\vec{D} = \epsilon_r \epsilon_0 \vec{E}$, and in all domains except the ferrite domain the constituent relationship for the magnetic flux density as $\vec{B} = \mu_r \mu_0 \vec{H}$. For the ferrite domain the relationship is given by Equation 6.17 which takes into account the magnetic moments represented by $\vec{M}$. The temw module maintains the appropriate boundary conditions while solving, e.g. continuity of magnetic flux density $\vec{B}$.

$$\vec{B} = \mu_0 \left(\vec{H} + \vec{M}\right) \tag{6.17}$$

A 25 kV pulse step pulse with a 500 rise time is applied to a 38.1 cm NLTL via a 50 Ω Lumped Port and the voltages of both the input port and output port are measured. The results of a simulation run using the parameters given in Table 6.1 are shown in Figures 6.4-6.6.

In Figure 6.4 the three magnetization components are plotted a single point as

Table 6.1: COMSOL Settings

Parameter	Value
Pulse Voltage	25 kV
Rise Time	500 ps
M_S	22 kA/m
Bias Field	25 kA/m
Geometry	2D axi-symmetric
Time Step	10 ps
Mesh Size	0.76 mm
Solver Mode	Fully Coupled
Solver	Direct: MUMPS
Solution Time	1 hr, 56 min, 22 s

a function of time. The point is located at the radial midpoint of the ferrite and the midpoint of the line (red point in Figure 6.3). The initial magnetization is $M_r = 0.1M_S$, $M_\phi = 0.1M_S$, and $M_z = 0.99M_S$. At the onset of the simulation the moments begin to align along $\vec{z}$ until the arrival of the voltage pulse at 2 ns at which time they begin to precess around the effective field.

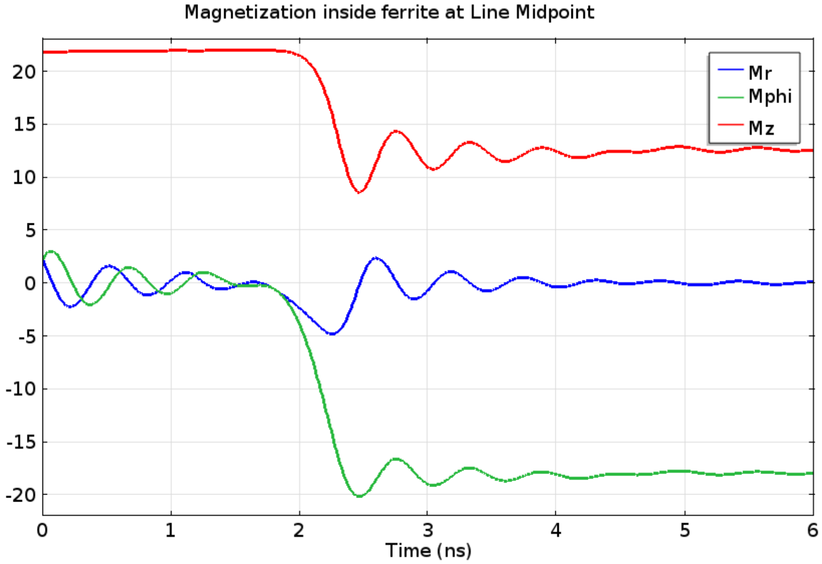

Figure 6.4: The power combiner can be represented as three transmission lines. When the signals on the input of the combiner are completely in phase the inputs can be treated as a single node, A, which will results in the input of the combiner, between A and B, looking like a single 25 Ω line.

The effect of the effective field on the oscillation frequency can be seen from Figure 6.5. The magnetization dynamics of the ϕ component of the magnetization are plotted for different radial distance in the ferrite at the line midpoint. The ϕ component is plotted since these moments will excite the transient modes that will propagate out of the line. The moments further from the center, red line labeled outer, see a lower effective field and accordingly have a lower frequency.

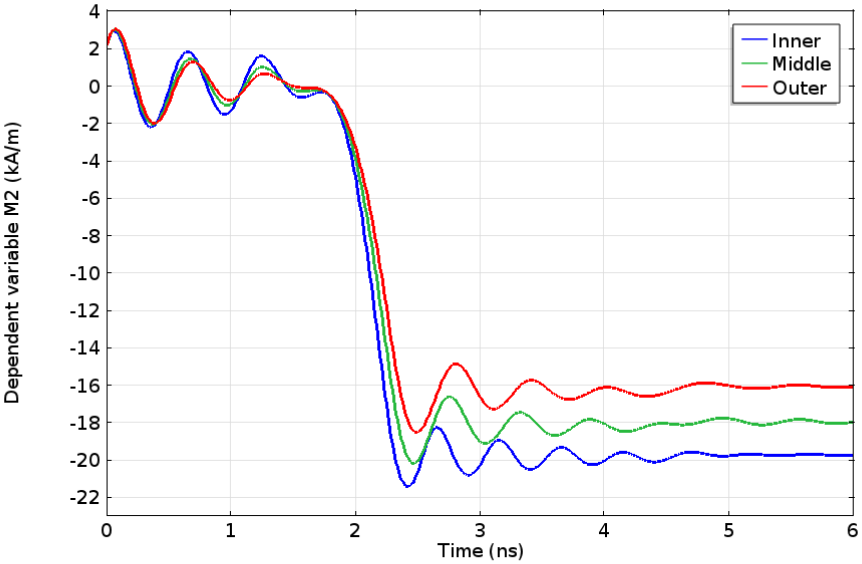

Figure 6.5: The azimuthal component M_ϕ of the magnetic moments taken at three radial points along the midpoint of the line. Each moment precesses at a different frequency due to the varying magnitude of the magnetic field.

Figure 6.6 shows the port voltages at the input and output of the line. A ripple can be seen at the beginning of the simulation on both ports, this is due to the moments settling along the $\vec{z}$ axis. The output voltage shown in green shows the microwave oscillations present on the output and the pulse sharpening effect expected.

The simulation has trouble dealing with values of spontaneous magnetization M_S that exceed the bias field. Since the constituent relationship inside the ferrite is given by Equation 6.17 it can be seen that their is a interdependence of the magnetic moment and the effective field it precesses about. When the precessing moments are large the simulation begins to runaway as the moments begin to move and begin changing the effect field, the bias field and transient voltage signal no longer set $\vec{H}_{eff}$

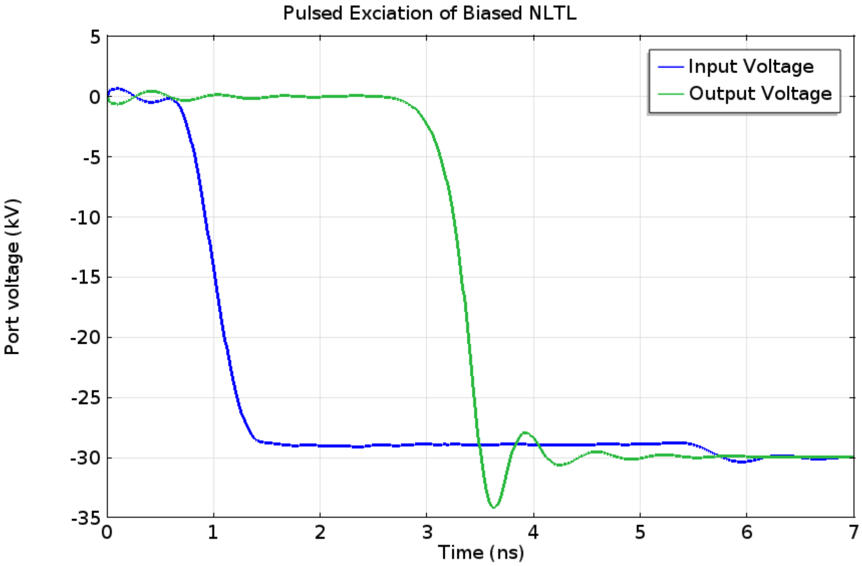

Figure 6.6: Input and output voltages for a negatively pulsed NLTL

at these high M_S values. This needs to be addressed since the values of M_S are of the order of 200 kA/m which greatly exceeds the bias field which typically range from 10 kA/m to 35 kA/m. The requirement to run with a low value of M_S explains the lower microwave oscillations than experimentally observed. Attempt to remedy the problem have include reduction in time step, reducing the mesh size, using iterative solvers, and recalculating the Jacobian on every solver iteration.

CHAPTER 7

CONCLUSIONS

A study of Coaxial Gyromagnetic Nonlinear Transmission Lines as High Power Microwave sources was conducted including the evaluation of ferrimagnetic materials, empirical line length testing for microwave generation, evaluation of solid dielectric materials, and testing of a high power combiner. A TEM horn was designed to radiate the NLTL output and evaluate the application of an array of NLTLs.

Several ferrites were tested for use in NLTLs including NiZn, Lithium, and YIG. The ferrite tested yielded viable ferrites for operation in the 10 kV range opening the possibility of using commercial solid state pulsers as the primary excitation source.

The empirical data gathered on line length dispels the minimum line length requirements previously assumed. Peak microwave powers are achieved in the 0.5 - 0.7 m range however microwaves are seen as low as 10 cm. This allows for the future development of more compact HPM systems.

Solid dielectrics have been proven as a viable insulator in NLTLs and have demonstrated the effectiveness of field shaping to improve NLTL performance. Insights into the magnetic field redistribution inside the ferrimagnetic material allow for the possibility of tuning NLTL output bandwidth by manipulation of the magnetic field gradient.

A high power transient combiner was demonstrated that performed as well as simulated. This has demonstrated the capability of precise control of NLTL delay via a simple bias field control scheme and led to further work on phased arrays of NLTLs.

An array of NLTLs was built and tested using a custom TEM horn design that demonstrated effective power combination in the far field.

A full field FEM simulation was created using COMSOL to evaluate performance of NLTLs. The simulation confirms the gyromagnetic excitation and propagation method of microwave generation of in coaxial NLTLs and provides insights into the magnetic field distribution inside the ferrimagnetic material. Future improvements on the simulation to overcome the limitation of simulating material with high saturation magnetization values will allow evaluation of new materials before fabrication.

REFERENCES

[1] Joachim Stohr and Hans Christoph Siegmann. *Magnetism.* Springer Berlin Heidelberg, 2006.

[2] Gerald F. Dionne. *Magnetic Oxides.* Springer, 2009.

[3] Benjamin Lax and Kenneth J. Button. *Microwave Ferrites and Ferrimagnetics.* McGraw-Hill, 1962.

[4] David M. Pozar. *Microwave Engineering.* Wiley, 2004.

[5] Hansjoachim Bluhm. *Pulsed power systems principles and applications.* Springer, Berlin, 2006.

[6] Helmut Kronmuller and Stuart Parkin, editors. *Handbook of Magnetism and Advanced Magnetic Materials: Volume 2 Micromagnetism.* Wiley, 2007.

[7] A. S. Gilmour. *Klystrons, Traveling Wave Tubes, Magnetrons, Cross-Field Amplifiers, and Gyrotrons (Artech House Microwave Library).* Artech House, 2011.

[8] James Benford, John A. Swegle, and Edl Schamiloglu. *High Power Microwaves, Second Edition (Series in Plasma Physics).* Taylor & Francis, 2007.

[9] J E Dolan and H R Bolton. Shock front development in ferrite-loaded coaxial lines with axial bias. *IEE Proceedings on Science, Measurement and Technology,* 147(5), 2000.

[10] James-William Braxton Bragg. *Ferrimagnetic-Based, Coaxial Nonlinear Transmission Lines.* PhD thesis, Texas Tech University, 2013.

[11] David K. Cheng. *Field and Wave Electromagnetics (2nd Edition).* Addison-Wesley, 1989.

[12] Robert M. White. *Quantum Theory of Magnetism.* Springer, 2006.

[13] John Jackson. *Classical electrodynamics*. Wiley, New York, 1999.

[14] Harry Suhl. *Relaxation Processes in Micromagnetics (International Series of Monographs on Physics)*. Oxford University Press, USA, 2007.

[15] *Ferrite Materials: Science and Technology*. Springer, 1991.

[16] Helmut Kronmuller. *Micromagnetism and the microstructure of ferromagnetic solids*. Cambridge Univ. Press, Cambridge u.a, 2003.

[17] G. A. Mesyatz. *Pulsed Power*. Kluwer Academic/Plenum Publishers, New York, 2005.

[18] S.J. MacGregor, F.A. Tuema, S.M. Turnbull, and O. Farish. The influence of polarity on trigatron switching performance. *IEEE Transactions on Plasma Science*, 25(2):118–123, Apr 1997.

[19] N. Trinh. Electrode design for testing in uniform field gaps. *IEEE Transactions on Power Apparatus and Systems*, PAS-99(3):1235–1242, May 1980.

[20] Warren L. Stutzman and Gary A. Thiele. *Antenna Theory and Design*. Wiley, 1997.

[21] Kenneth R. Demarest. *Engineering Electromagnetics*. Lebanon, Indiana, U.S.A.: Prentice Hall, 1998.

[22] James-William Braxton Bragg. Investigation of ferrite-filled coaxial nonlinear transmission lines for high power microwave generation. Master's thesis, Texas Tech University, 2010.

[23] J.-W. B. Bragg, J. C. Dickens, and A. A. Neuber. Material selection considerations for coaxial, ferrimagnetic-based nonlinear transmission lines. *Journal of Applied Physics*, 113(6):064904, 2013.

[24] Ilya V. Romanchenko, Vladislav V. Rostov, Vladimir P. Gubanov, Alexey S. Stepchenko, Alexander V. Gunin, and Ivan K. Kurkan. Repetitive sub-gigawatt rf source based on gyromagnetic nonlinear transmission line. *Review of Scientific Instruments*, 83(7):074705, 2012.

[25] Dirk I. L. de Villiers, Pieter W. van der Walt, and Petrie Meyer. Design of a Ten-Way Conical Transmission Line Power Combiner. *IEEE Transactions on Microwave Theory and Techniques*, 55(2):302–308, February 2007.

[26] A.E. Fathy and David Kalokitis. A simplified design approach for radial power combiners. *IEEE Transactions on Microwave Theory and Techniques*, 54(1):247–255, January 2006.

[27] J. Duncan and V. Minerva. 100:1 Bandwidth Balun Transformer. *Proceedings of the IRE*, 48(2):156–164, February 1960.

APPENDIX A: Calibration of Capacitive Voltage Probes

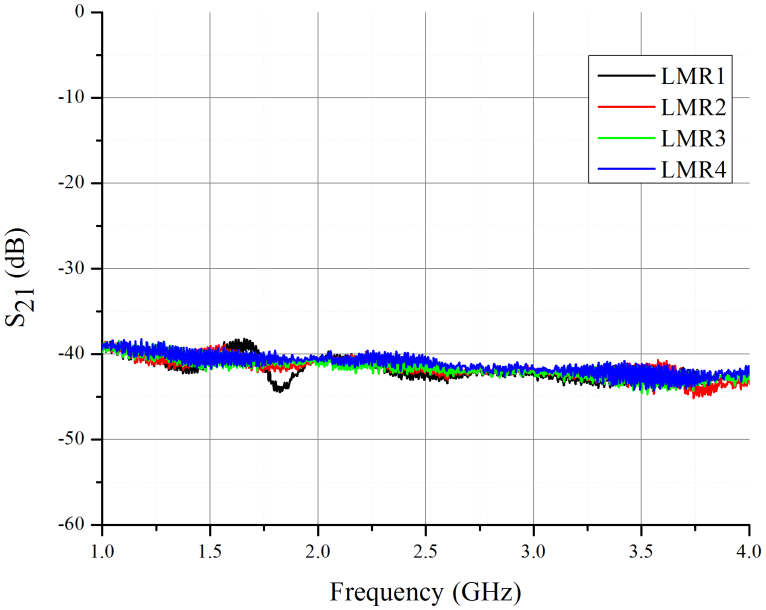

Figure A.1: Calibration of the LMR-600 based CVP using the Network Analyzer.

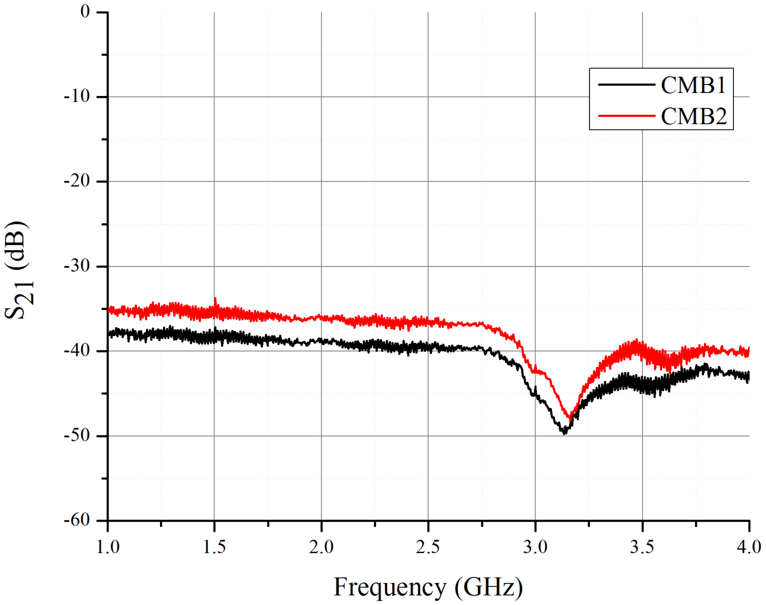

Figure A.2: Calibration of the CVPs on the input of the transient power combiner using the Network Analyzer.